iScience

CellPress
OPEN ACCESS

Article

Anion-Modulated Platinum for High-Performance Multifunctional Electrocatalysis toward HER, HOR, and ORR

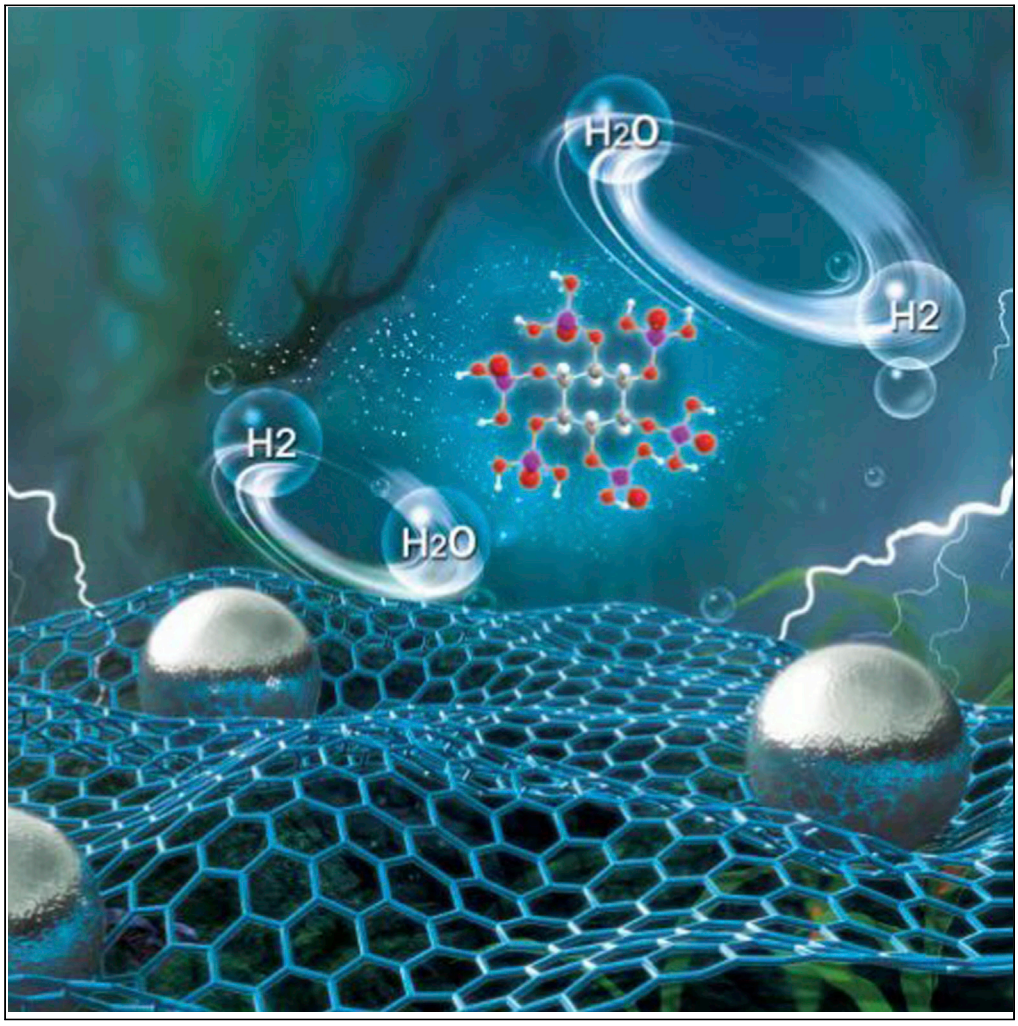

Zonghua Pu, Ruilin Cheng, Jiahuan Zhao, ..., , Ding Chen, Shichun Mu

msc@whut.edu.cn

HIGHLIGHTS

PtP_2@PNC is synthesized under ambient pressure and moderate temperatures

The formed PtP_2@PNC exhibits outstanding performance toward HER, HOR, and ORR

The synergistic effect between PtP_2 and PNC is responsible for the high activity

Pu et al., iScience *23*, 101793
December 18, 2020
https://doi.org/10.1016/j.isci.2020.101793

iScience

CellPress
OPEN ACCESS

Article

Anion-Modulated Platinum for High-Performance Multifunctional Electrocatalysis toward HER, HOR, and ORR

Zonghua Pu,[1,2] Ruilin Cheng,[1] Jiahuan Zhao,[1] Zhiyi Hu,[3] Chaofan Li,[3] Wenqiang Li,[1] Pengyan Wang,[1] Ibrahim Saana Amiinu,[1] Zhe Wang,[1] Min Wang,[1] Ding Chen,[1] and Shichun Mu[1,2,4,*]

SUMMARY

Efficient electrocatalyst toward hydrogen evolution/oxidation reactions (HER/HOR) and oxygen reduction reaction (ORR) is desirable for water splitting, fuel cells, etc. Herein, we report an advanced platinum phosphide (PtP_2) material with only 3.5 wt % Pt loading embedded in phosphorus and nitrogen dual-doped carbon (PNC) layer (PtP_2@PNC). The obtained catalyst exhibits robust HER, HOR, and ORR performance. For the HER, a much low overpotential of 8 mV is required to achieve the current density of 10 mA cm^{-2} compared with Pt/C (22 mV). For the HOR, its mass activity (MA) at an overpotential of 40 mV is 2.3-fold over that of the Pt/C catalyst. Interestingly, PtP_2@PNC also shows exceptional ORR MA which is 2.6 times higher than that of Pt/C and has robust stability in alkaline solutions. Undoubtedly, this work reveals that PtP_2@PNC can be employed as nanocatalysts with an impressive catalytic activity and stability for broad applications in electrocatalysis.

INTRODUCTION

The increasing requirement for clean, eco-friendly, and sustainable energy has prompted the development of energy technologies to focus more on renewability, efficiency, and environmental protection (Steele et al., 2001; Zhang et al., 2016a, 2016b; Mallouk et al., 2013). In view of its unique properties, hydrogen perfectly accords with those requirements, thus making it the most promising candidate to replace fossil fuels in the future. Undoubtedly, among those hydrogen generation technologies, electrochemical water splitting is an important method, meanwhile hydrogen evolution reaction (HER) is a vital kinetic process of electrochemical water splitting (Balat et al., 2009; Turner, 2004). Besides, efficient hydrogen oxidation reaction (HOR) and oxygen reduction reaction (ORR) can improve the energy efficiency, which also plays an important role in the sustainable energy devices, especially for fuel cells and metal-air batteries (Lee et al., 2011; Huang et al., 2015). However, on the one hand, the sluggish kinetics of ORR generally requires a large overpotential to drive the reaction. On the other hand, it is challenging but urgent to rationally design a practical and efficient electrocatalyst with better performance and lower cost. In addition, alternative electrocatalysts for HER, HOR, and ORR with various structures and chemical compositions have already been widely explored (such as precious metals, non-noble metals, and even metal-free materials) (Zheng et al., 2014a, 2014b, 2016; Huang et al., 2017; Shan et al., 2019; Liu et al., 2014; Popczun et al., 2013; Morales-Guio et al., 2014; Bu et al., 2017; Ma et al., 2015; Zhu et al., 2017). However, Pt group metal-based (PGM-based) catalysts are still the best materials for these electrocatalytic reactions. Their high cost, scarcity, and poor stability of PGM-based catalysts have driven efforts to reduce Pt usage toward their commercialization in energy devices.

During the past few years, intense investigations have been made in this field and a bunch of optimized strategies has been designed to lower the Pt loading and improve utilization efficiency. Among those strategies, the most widely applied method to reach this significant challenging goal is to alloy Pt together with other low-cost 3d transition metals (Tian et al., 2020a, 2020b; Wu et al., 2013; Porter et al., 2013). Owing to the optimized structure and electronic effects caused by M (M = Fe, Co, Ni, Cu, Cr, Ti, V, Pb, Mn, etc.), the PtM alloys present significant potentials in improving the electrochemical activity for a series of catalytic reactions (such as HER, ORR, methanol/ethanol oxidation reaction [MOR or EOR]) (Huang et al., 2017; Bu et al., 2017; Li et al., 2018; Cui et al., 2014; Ma et al., 2020a, 2020b; Wang et al., 2017; Ma et al.,

[1]State Key Laboratory of Advanced Technology for Materials Synthesis and Processing, Wuhan University of Technology, Wuhan 430070, P. R. China

[2]Foshan Xianhu Laboratory of the Advanced Energy Science and Technology Guangdong Laboratory, Xianhu Hydrogen Valley, Foshan 528200, China

[3]Nanostructure Research Centre, Wuhan University of Technology, Wuhan 430070, China

[4]Lead Contact

*Correspondence: msc@whut.edu.cn

https://doi.org/10.1016/j.isci.2020.101793

2020a, 2020b; Fan et al., 2016). Nevertheless, the M in the PtM-based nanoparticles (NPs) is inclined to dissolve during the highly oxidizing and/or acidic environment, which is inevitable to degrade proton exchange membranes in fuel cells or to deteriorate the electrolyte solutions in water splitting during the practical application (Wang et al., 2011; Wang et al., 2015; Wang et al., 2018a, 2018b; Dubau et al., 2011).

It is worth noting that previous researches usually focus on 3d transition metal alloying Pt. However, the long-term durability of alloy catalysts, due to the second metal dissolution and particle growth, still remains a huge challenge (Cui et al., 2015a, 2015b). In addition, for disordered Pt alloying M structure, the atomic positions are occupied randomly by M and Pt. Thus, the Pt alloy has randomly distributed active centers and changing surface composition. Oppositely, if Pt combines anions (such as P, S, Se, Te) and forms Pt compounds that have a fixed crystal structure, provide predictable control of the structure. As an example, non-metal P anion combination in Pt formed platinum phosphide (PtP_2) has been rarely reported but is expected to improve the intrinsic activity of electrocatalysts, because P atoms with more electronegativity can grab electrons from Pt atoms, significantly tuning the compound electronic structure (Shi and Zhang, 2016). More importantly, for transition metal phosphides (TMPs), it is reported that improving the atomic percentage of P may significantly enhance HER activity. Additionally, to further improve the dispersibility and stability of metal compounds, the heteroatoms (N, P, S, etc.)-doped carbon materials are generally used as the support of metal compounds, which can effectively prevent the migration and aggregation of NPs. At the same time, such heteroatom-doped carbon materials are able to synergistically boost the activities of metal compounds-based catalysts.

Inspired by the above-mentioned description, in this work, PtP_2 NPs are fabricated at moderate temperatures and ambient pressure in terms of P, N dual-doped carbon layer (PNC) encapsulation (PtP_2@PNC). As expected, the PtP_2@PNC catalyst with a low Pt mass loading (3.5 wt %) exhibits outstanding HER, HOR, and ORR, performance even better than commercial Pt/C (20 wt %). On the one hand, the high catalytic activity can be attributed to that the negatively charged P atoms can catch electrons from Pt atoms, significantly tuning the compound electronic structure, and therefore enhancing the Pt activity. On the other hand, the unique structural relationship of the P, N dual-doped C mainly provides a protective shield to inhibit PtP_2 migration and agglomeration, as well as facilitate the conductivity and charge/mass transport in the materials during the electrochemical process.

RESULT AND DISCUSSION

As illustrated in Figure 1, PtP_2@PNC was fabricated by a facile pyrolysis method. First, phytic acid (PA) cross-linked platinum complexes (PtPA) were formed based on the strong chelating ability of PA (Tian et al., 2020a, 2020b; Zhou et al., 2019). Then, PtPA-dicyandiamide supermolecular aggregate was produced via a simple cooperative assembly process in water at room temperature (Zhang et al., 2016a, 2016b). Finally, the PtP_2 NPs embedded in PNC layers were obtained by a thermal treatment of the PtPA-dicyandiamide precursor at 900°C under Ar atmosphere. It is worth noting that, without introducing the PA precursor in our experiments, only Pt nanoparticles supported on N-doped carbon (Pt-NC) was obtained (Figure S1). That is, PA plays an important role in the TMPs preparation process and can be used as a green phosphorus source. As a reference, PNC layers also can be prepared by the same synthesis strategy but without adding the H_2PtCl_6 precursor (Figures S2–S4). The formation of PNC layers can be described to the presence of P- and N-containing functional groups in the PA and dicyandiamide precursors during the carbonization process, leading to simultaneous self-doping of P and N into the carbon layers. Furthermore, PNC-supported Pt (Pt-PNC) has also been prepared by using the similar method (Figure S5).

The obtained product was first characterized by powder XRD. As displayed in Figure 2A, the 2θ peaks at 27.1°, 31.4°, 44.9°, 53.3°, 55.9°, 72.2°, and 74.4° are assigned to the (111), (200), (220), (311), (222), (331), and (420) crystal planes, respectively, indicating a typical crystalline cubic PtP_2 phase (PDF No. 65-0004, space group: Pa-3, $a_o = b_o = c_o = 5.695$ Å). Subsequently, XPS was carried out and illustrated in Figures 2B–2F. The survey scan (Figure 2B) shows the presence of all elemental components including Pt, P, C, N, and O. The fitting spectra of Pt4f indicate four peaks, corresponding to oxidized Pt and Pt. The peaks located at 71.6 and 74.9 eV are assigned to $Pt4f_{7/2}$ and $Pt4f_{5/2}$ of Pt (Figure 2C) (Kalinkin et al., 2010; Yang et al., 2018). Compared with $Pt4f_{7/2}$ peak located at 71.1 eV of metallic Pt, the binding energy (BE) in PtP_2@PNC is positive shifted, suggesting Pt in PtP_2@PNC exhibits a slightly positive charge (δ+). The rest of two peaks at 73.2 and 76.5 eV are ascribed to the oxidized Pt. Regarding P2p core-level spectra (Figure 2D), the subpeaks at 133.4 and 132.5 eV are attributed to the presence of P-O and P-C species, as well as

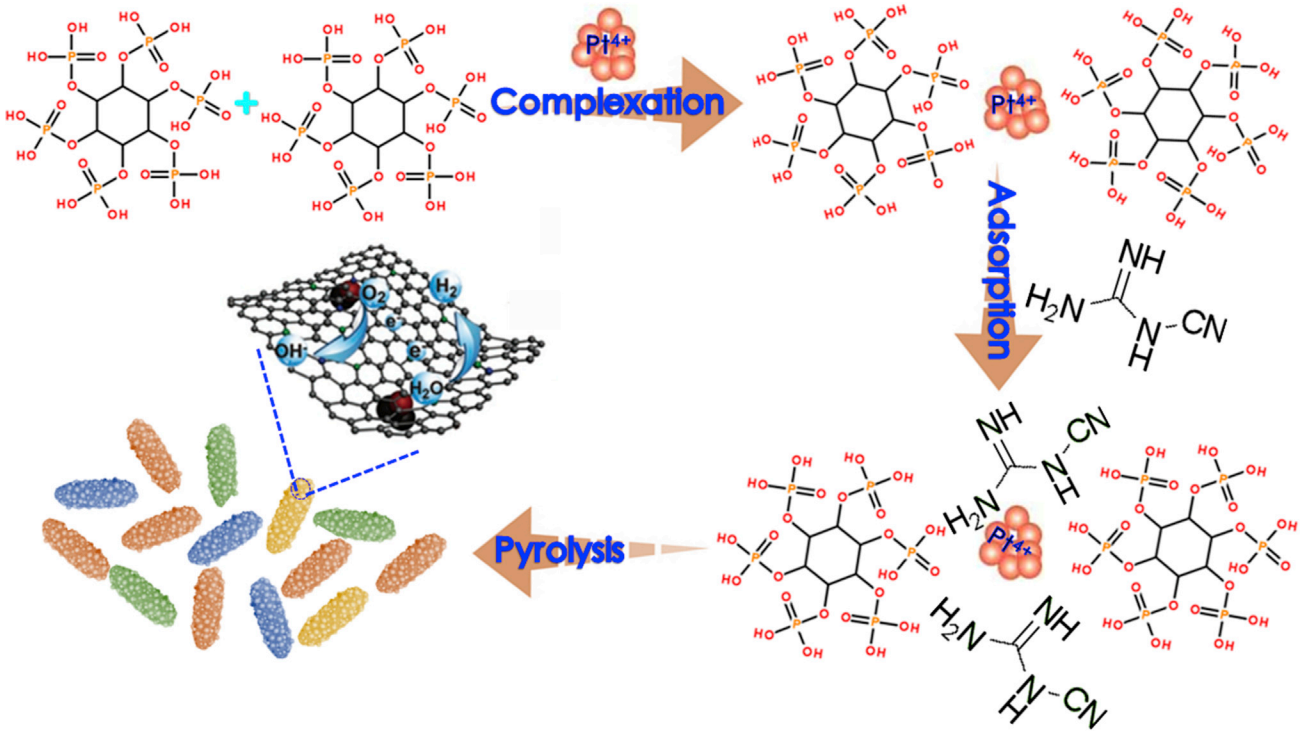

Figure 1. Schematic Illustration of the Synthesis of PtP_2@PNC Catalysts

two weak subpeaks observed at about 129.3 and 130.2 eV are assigned to the Pt–P bond, suggesting a successful formation of PtP_2@PNC (Zhang et al., 2015). The BE of 129.3 eV for P $2p_{3/2}$ exhibits a negative shift from that of P^0 (130.2 eV) (Tian et al., 2020a, 2020b), which indicates that P is negative charge (δ–). These results points to weak electron density transfer from Pt to P in the PtP_2@PNC.

The N 1s spectrum (Figure 2E) can be fitted into three separated peaks with binding energies (BEs) at 398.6. 400.5, and 401.2 eV corresponding to pyridinic-N, pyrrolic-N, and graphitic-N species, respectively. As reported, graphitic-N is considered to improve the diffusion-limited properties, while pyridinic-N, as an active site for ORR, boosts the onset potential, electrical conductivity, and surface wettability (Amiinu et al., 2017; Zhao et al., 2013). In addition, it is demonstrated that pyridinic-N, pyrrolic-N, and graphitic-N species are beneficial for HER electrocatalysis (Zheng et al., 2014a, 2014b). The C 1s XPS spectrum (Figure 2F) demonstrates the existence of C=C (284.6 eV), C–O/C–N/C–P (285.9 eV), C=O/C=N (286.4 eV), and C–C=O (289.3 eV) bonds in PtP_2@PNC. It should be noteworthy that the aforementioned C–P and C–N bonding further indicate the successful doping of P and N into carbon layers. In addition, the carbon component was further characterized by the Raman spectrum. As illustrated in Figure S6, two strong peaks at ~1,345 and 1,598 cm^{-1} are corresponded to the D- and G-band, respectively. The intensity ratio of I_D/I_G is found to be 1.04, indicating that the PtP_2@PNC sample contains many defective carbons. Moreover, the content of Pt loaded on PNC is confirmed to be about 3.5 wt % by ICP-AES.

The morphology of PtP_2@PNC was characterized by SEM and TEM. As shown in Figure S7A, numerous carbon nanosheets are observed from the SEM images. The low- and high-magnification TEM images of PtP_2@PNC indicate homogeneous dispersion of PtP_2 NPs in PNC layers (Figures S7B and 2G). High-angle annular dark-field scanning TEM (HAADF-STEM) further clearly demonstrates the presence of numerous small PtP_2 NPs (Figure 2H). As shown in Figures S8 and S9, the average size of the PtP_2 NPs is about 11.7 ± 2.5 nm (~100 nanoparticles were measured). The lattice fringe with an interplanar distance of 3.288 Å is clearly displayed in the high-resolution TEM (HRTEM) image (Figure 2I), corresponding to the (111) facet of cubic PtP_2 phase. Additionally, the fast Fourier transform (FFT) pattern (Figure S10B) deriving from the PtP_2 (circled in Figure S10A) verifies the existence of (311), (211), and (200) facets. The HRTEM images in Figures 3A and 3B further reveal that PtP_2 NPs are embedded within P and N dual-doped carbon

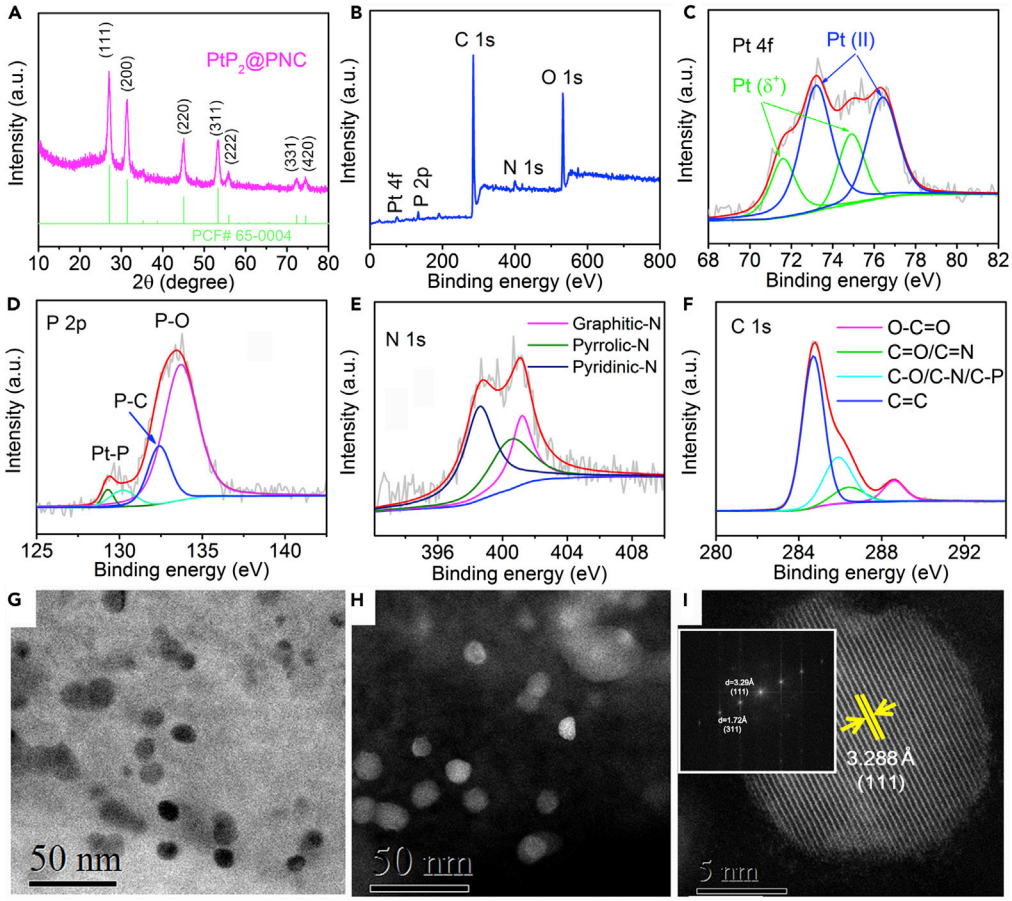

Figure 2. Structure and Microscopy Characterization of PtP_2@PNC

(A) XRD pattern of PtP_2@PNC catalysts.

(B–F) XPS spectra of (B) survey scan, (C) Pt 4f regions, (D) P 2p regions, (E) N 1s regions, and (F) C 1s regions for PtP_2@PNC.

(G–I) (G) TEM, (H) HAADF-STEM, and (I) HRTEM images of PtP_2@PNC (inset: corresponding FFT pattern).

with ~1–6 layers (PNC layers are indicated by the white arrows). Simultaneously, HAADF-STEM and the corresponding energy dispersive spectrometer (EDS) elemental mappings (Figure 3C) distinctly confirm the homogeneous distributions of C, N, Pt, and P elementals. All of these characterizations (XRD, XPS, and TEM) indicate that PtP_2@PNC was successfully achieved.

HER tests were evaluated in H_2-saturated acid solutions (0.5 M H_2SO_4) in a two-compartment, three-electrode cell with a scan rate of 5 mV s^{-1}. All the LSVs curves were not *iR* corrected. Before the tests, the saturated calomel electrode (SCE) was calibrated by continually bubbling the solution (0.5 M H_2SO_4) with ~1 atm of research-grade H_2 (g) using a clean platinum electrode as the working electrode (Figure S11). As shown in Figure 4A nearly zero onset potential is observed for both PtP_2@PNC and commercial Pt/C. To attain the current density (j) of 10 milliamperes per square centimeter (mA cm^{-2}), the catalyst for PtP_2@PNC only needs a much lower overpotential (8, 12 mV without iR correction, Figure S12) compared with commercial Pt/C (22 mV). Furthermore, to the best of our knowledge, the HER performance of PtP_2@PNC is superior to the PNC layers (183 mV @ 10 mA cm^{-2}), Pt-PNC (19 mV @ 10 mA cm^{-2}), Pt-NC (59 mV @ 10 mA cm^{-2}) and all of the noble-metals, non-precious metal-based catalysts as well as non-metal HER catalysts (Figures S13, 14, and 4B and Table S1). Tafel analysis of the PtP_2@PNC nanomaterial in 0.5 M H_2SO_4 indicates a Tafel slope of ~30 mV dec^{-1} in the region of η = 5–30 mV (Figure 4C). This value is consistent with the known mechanism of the HER on commercial Pt/C. At higher overpotentials (η = 60–100 mV), the Tafel slope increased to ~122 mV dec^{-1}. This value does not match the expected Tafel slopes of 29, 38, and 116 mV dec^{-1}, each of which correlates with a different rate-determining step of the HER. Furthermore, Figure S15 displays the electrochemical impedance

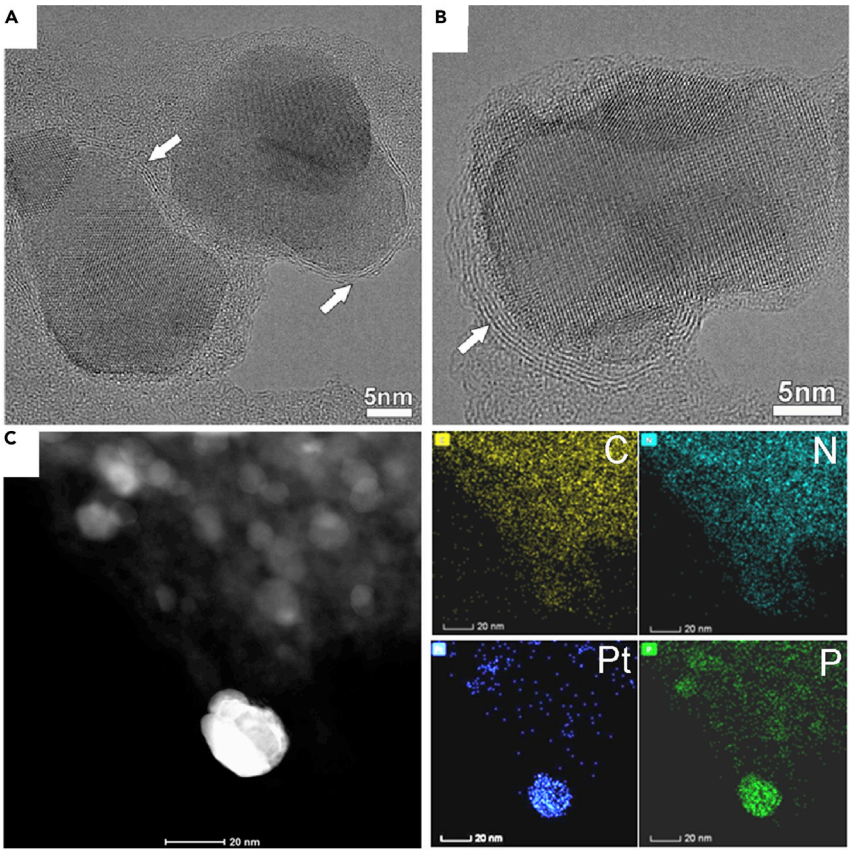

Figure 3. Microscopy Characterization of PtP_2@PNC

(A–C) (A and B) HRTEM images of PtP_2@PNC and PNC are indicated by the white arrows. (C) HAADF-STEM image and corresponding EDX elemental maps of C (yellow), N (cyan), Pt (blue), P (green).

spectroscopy (EIS) data of different samples. From the plots, we can learn that PtP_2@PNC shows more favorable HER kinetics.

Besides the high HER catalytic activity, stability is also another important parameter to promote the materials' practical application. As shown in Figure 4D, PtP_2@PNC presents good stability with a slight degradation of the current density even after 24 h of the continuous electrochemical scan. Similarly, it also maintains high activity after being subjected to an accelerated degradation test for certain CV cycles (Figure 4E). It presents that PtP_2@PNC can sustain the current density of 10 mA cm^{-2} with only a small potential degradation ~3 mV after 2,000 CV cycles, whereas the commercial Pt/C deteriorates by ≈ 6 mV even after 1,000 CV cycles (Figure 4F), indicating the superior durability for the PtP_2/PNC catalyst. To further evaluate the catalyst durability, we conducted both TEM and XPS analysis of PtP_2@PNC after electrochemical stability tests. As illustrated in Figure S16, the TEM image shows that the PtP_2 NPs still maintain good dispersion without obvious migration and aggregation owing to the robust thin PNC layers entrapment. More importantly, the similarity of high-resolution Pt4f, P2p, N1s, and C1s XPS spectra (Figure S17) of the fresh and post-HER PtP_2@PNC materials further demonstrates the retention of the materials in terms of composition, confirming its outstanding robustness for HER electrocatalysis. However, after the HER stability test, part of P species is detected in the electrolyte by the ICP-AES (Table S2), possibly caused by the detachment of the catalyst from the electrode surface due to the vigorous gas evolution (Andronescu et al., 2017). Furthermore, the HER activity of PtP_2@PNC in neutral and alkaline media was also investigated. As shown in Figure S18, the PtP_2@PNC materials also show nearly commercial Pt/C activity under neutral and alkaline conditions. Specifically, to reach the current density of 10 mA cm^{-2}, PtP_2@PNC requires overpotentials of 64 and 45 mV in 1.0 M phosphate buffered saline (PBS) and 1.0 M KOH solutions, respectively. All of the above results suggest that PtP_2@PNC possesses Pt-like HER catalytic performance under multi-pH conditions.

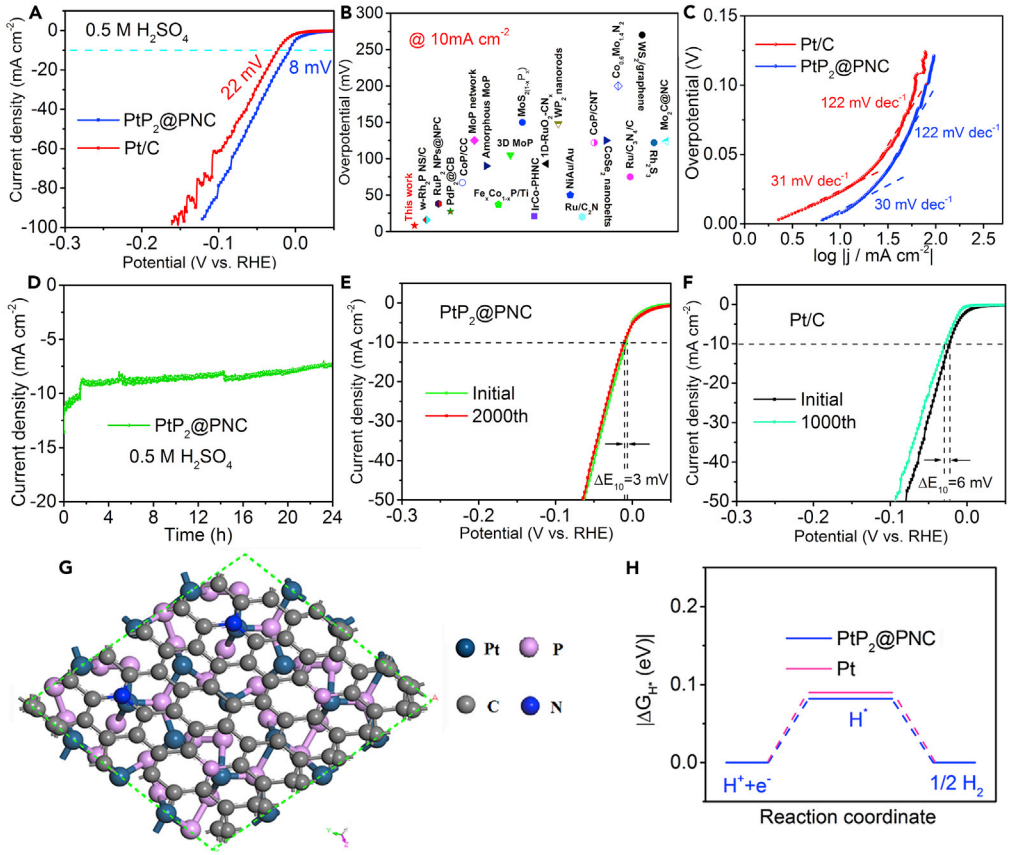

Figure 4. HER Activities of PtP_2@PNC and Commercial Pt/C

(A–F) (A) HER polarization curves for PtP_2@PNC and commercial Pt/C recorded at 5 mV s^{-1}. (B) The HER activity comparison between PtP_2@PNC with other HER catalyst, references are detailed in Table S1. (C) Corresponding Tafel slops. (D) Time-dependent current density curve of the PtP_2@PNC in 0.5 M H_2SO_4 (without iR correction). Polarization curves for (E) PtP_2@PNC and (F) commercial Pt/C initial and after 1,000 CV scanning between +0.1 and −0.2 V versus RHE. (G–H) (G) The theoretical model of PtP_2@PNC used in DFT calculations. (H) Calculated free energy diagram of the catalyst samples.

Based on the above results, the high HER performance of PtP_2@PNC can be ascribed to the following points. (1) As described in Figures 4G, 4H, and S19, when PtP_2 is incorporated with PNC, the resultant PtP_2@PNC yields an optimal adsorption free energy of H (ΔG_{H^*}), which is even lower than that of Pt, indicating that the introduction of P to Pt could weaken the binding energy between Pt and hydrogen atoms, which further facilitates the hydrogen evolution during the HER process (Robinson et al., 2017; Luo et al., 2018; Wang et al., 2018a, 2018b). (2) As evidenced by the XPS, the main Pt $4f_{7/2}$ peak in PtP_2@PNC is at 71.6 eV, representing positive shifts in the binding energies of +0.05 eV, compared with the binding energy of the Pt $4f_{7/2}$ peak in pure Pt (71.1 eV). This shows the electronic structure of metal Pt was changed after introducing P. In other words, negatively charged P atoms can capture electrons from Pt atoms and play an important role as Lewis base to work with positively charged protons in the HER process (Shi and Zhang, 2016; Guo et al., 2018; Zhuang et al., 2016). Like metal complex and [NiFe] hydrogenases catalysts, the P and Pt serve as the hydride-acceptor and proton-acceptor center, respectively, improving the HER catalytic activity (Popczun et al., 2013; Kibsgaard et al., 2014; Cui et al., 2015a, 2015b). (3) The PtP_2 NPs uniformly encapsulated in the PNC layers can effectively prevent the aggregation and migration of those PtP_2 active centers, thus endowing the PtP_2@PNC superior catalytic stability. (4) The presence of the PNC layer in the catalyst may further improve the conductivity of the PtP_2@PNC, therefore enhancing the electron transfer during the HER process. As reported P and/or N doping carbon could improve HER activity to some extent in comparison with pure carbon materials (Zhang et al., 2015; Zheng et al., 2014a, 2014b). In other words, the P, N dual-doped carbon materials are able to synergistically improve the activities of PtP_2@PNC

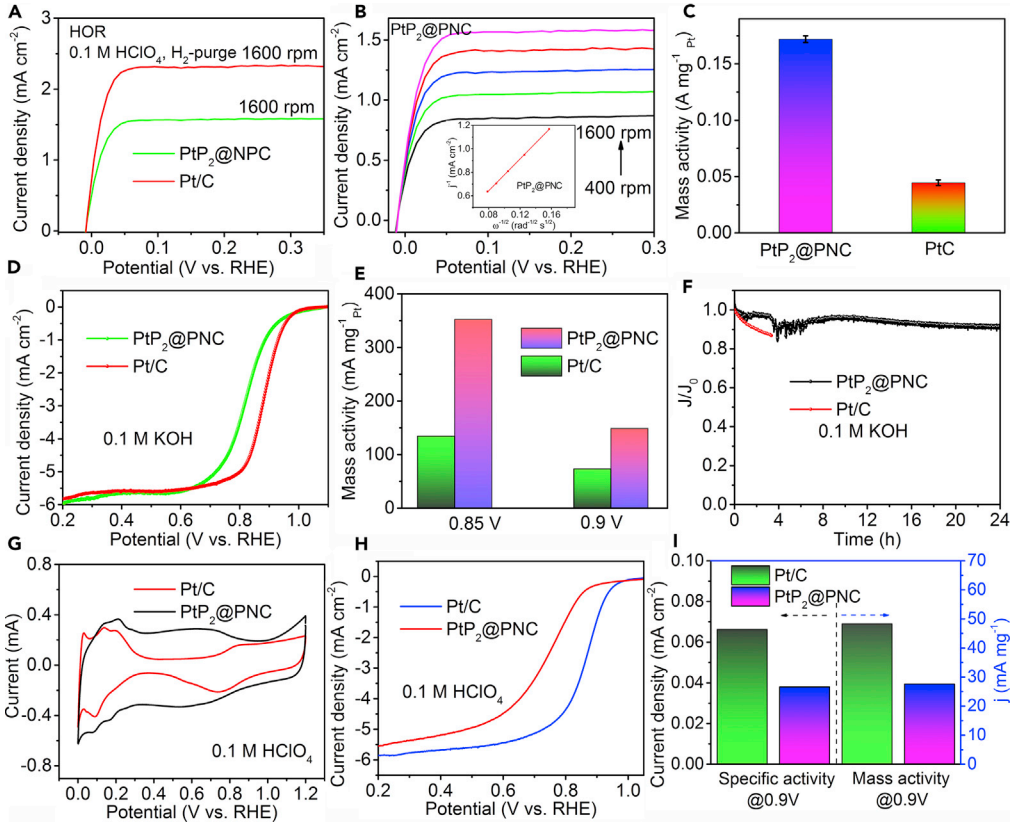

Figure 5. HOR and ORR Activities of PtP_2@PNC and Commercial Pt/C

(A–C) (A) Polarization curves of PtP_2@PNC and Pt/C for HOR in H_2-saturated 0.1 M $HClO_4$. (B) HOR polarization curves on PtP_2@PNC catalyst at different rotation rates from 400 to 1,600 rpm. The inset image shows a Koutecky-Levich plot at 0.15 V versus RHE. (C) Mass activity at 40 mV of the PtP_2@PNC and Pt/C.

(D–F) (D) LSV curves of PtP_2@PNC and commercial 20 wt % Pt/C catalyst at 5 mV s^{-1} at a rotating speed of 1,600 rpm obtained in O_2-saturated 0.1 M KOH solutions. (E) Mass activity of the Pt/C and PtP_2@PNC for ORR at 0.85 and 0.9 V, respectively. (F) Current versus time (i-t) chronoamperometric curves of the PtP_2@PNC and Pt/C at the rotation speed of 1,600 rpm and the constant potential of −0.3 V.

(G-I) (G) CVs of PtP_2@PNC and Pt/C in 0.1 M $HClO_4$ solutions. (H) LSV curves of PtP_2@PNC and commercial 20 wt % Pt/C catalysts at 5 mV s^{-1} at a rotating speed of 1,600 rpm obtained in O_2-saturated 0.1 M $HClO_4$ solutions. (I) Histogram of mass and specific activities of PtP_2@PNC and Pt/C electrocatalysts at 0.9 V versus RHE.

catalysts. Moreover, we conducted a band structure analysis to examine the electronic-coupling effect between PNC and PtP_2. As illustrated in Figure S20, pure PtP_2 displays a band gap of 0.3 eV, while coupling PtP_2 with PNC, the band gap of PtP_2@PNC is decreased to 0.087 eV. Therefore, after coupling PtP_2 with PNC, the charge density of the PtP_2@PNC is redistributed in the form of an apparent electron transfer from the conductive PNC to PtP_2, leading to electron enrichment of the PtP_2 layer. Besides, the total density of states (DOS) in PtP_2@PNC is quite different from that of PtP_2. These investigations further demonstrate that the coupling of PNC layers strongly influences the electronic structures of PtP_2 in the PtP_2@PNC by enhancing electron mobility and HER performance. (5) PtP_2@PNC has a high electrochemically active surface area (ECSA: ≈ 510 cm^2) (Figure S21), which can favor the effective accessibility of the intrinsic active sites. Such large ECSA benefits from the high BET specific surface area (≈159.3 m^2 g^{-1}) (Figure S22).

Additionally, it also remains a huge challenge in developing low-Pt HOR catalysts under the acidic condition for the widespread employment of proton-exchange membrane fuel cell (PEMFC). Therefore, the HOR activity for PtP_2@PNC was examined by using a rotating disk electrode (RDE) test with a scan rate of 2 mV s^{-1} in H_2-saturated 0.1 M $HClO_4$ solution. For comparison, we also tested the HOR activities of Pt-PNC and bare PNC (Figure S23). As shown in Figure 5A, the HOR mass activity (MA) of PtP_2@PNC is higher than that of commercial Pt/C. Figure 5B displays the HOR polarization curves on PtP_2@PNC at different rotating

speeds from 400 to 1,600 rpm. When the current is controlled by both reaction kinetics and H_2 diffusion, Koutecky-Levich equation applies (Hunt et al., 2016):

$$\frac{1}{J} = \frac{1}{J_l} + \frac{1}{J_k} = \frac{1}{J_k} + \frac{1}{B\omega^2} \quad \text{(Equation 1)}$$

$$B = 0.62nC_0D_0^{\frac{2}{3}}\nu^{\frac{-1}{6}} \quad \text{(Equation 2)}$$

$$J_k = nFkxC_0 \quad \text{(Equation 3)}$$

where J, J_l, and J_K are the measured, kinetic, and diffusional current densities, respectively. F is the Faraday constant, D_0 is the diffusivity (4.5×10^{-5} $cm^2 \cdot s^{-1}$) of hydrogen in 0.1 M $HClO_4$, n is the electron transfer number in HOR, ν is the kinetic viscosity of the electrolyte (0.008 $cm^2 \cdot s^{-1}$), C_0 is the solubility of hydrogen in 0.1 M $HClO_4$ (7.2×10^{-7} $mol \cdot cm^{-3}$), and ω is the rotating speed. By fitting the data at an overpotential of 0.15 V with Equations (1)–(3), a linear plot of $\omega^{-1/2}$ with j^{-1} was obtained (inset of Figure 5B). The slope is 5.49 cm^2 $mA^{-1} \cdot s^{-1/2}$, which is reasonably closed to the two-electron transfer of HOR. Furthermore, as illustrated in Figure 5C, the corresponding MA of PtP_2@PNC and commercial Pt/C were calculated by the loading amount of Pt metal, respectively. The MA value for PtP_2@PNC is 0.172 A mg^{-1}_{Pt}, which is nearly 2.3 times greater than that of the commercial Pt/C (0.074 A mg^{-1}_{Pt} for MA). In fact, ΔG_{H^*} is also an important descriptor for HOR (Wang et al., 2019). According to the Sabatier principle, ideal HOR electrocatalysts should have ΔG_{H^*} close to zero. The $|\Delta G_{H^*}|$ value is calculated to be 0.09 eV on Pt(111) from density functional theory (DFT) calculations. As for PtP_2@PNC, the $|\Delta G_{H^*}|$ is lower than that of Pt, indicating that the introduction of P to Pt could weaken the hydrogen adsorption. All of these indicate that PtP_2@PNC is a promising HOR catalyst in acidic electrolytes for the widespread employment of PEMFC.

To investigate the multifunctional catalytic activities, we also probed the ORR activity of the PtP_2@PNC samples in basic solutions. LSVs were measured to investigate the kinetics and mechanism of PtP_2@PNC in O_2-saturated basic solutions (0.1 M KOH) at a rotation rate of 1,600 rpm (Figure 5D). Its onset and half-wave potentials for PtP_2@PNC is about 0.97 and 0.82 V, respectively, which exhibits nearly identical ORR activity compared with the 20 wt % commercial Pt/C. However, owing to the limited 3.5 wt % content of Pt in PtP_2@PNC, the MA of PtP_2@PNC is far greater than that of commercial Pt/C. As illustrated in Figure 5E, PtP_2@PNC further exhibits a remarkable MA at 0.85 and 0.9 V, which is nearly 2.6 and 2.0 times higher than that of commercial Pt/C. Additionally, compared with PtP_2@PNC, PNC layers and Pt-PNC show an even worse ORR activity, as confirmed by their more negative onset potential and lower steady-state current density (Figures S24 and S25). To further investigate the ORR kinetics, the LSVs of PtP_2@PNC were scanned at different rotating speeds from 400 to 2,000 rpm (Figure S26A). Koutecky-Levich plots (J^{-1} versus $\omega^{-1/2}$) were obtained to better understand the number of electrons transferred (n) during ORR (inset of Figure S26B). And the calculated n value of PtP_2@PNC is approximately equal to 3.96, which confirms the preferred four-electron transfer reaction for PtP_2@PNC during the ORR process (Zhang et al., 2015; Greeley et al., 2019; Wang et al., 2012). In addition, to understand the possible mechanism for the improved ORR performance of PtP_2@PNC, DFT calculations were also carried out. The O_2 adsorption energy (ΔE_{O2}) on Pt is 3.3 eV (Figure S27), which is larger than that on PtP_2@PNC (1.8 eV). In other words, there is easier desorption of oxygen molecules on PtP_2@PNC than on Pt, further enhancing the O_2 reduction performance.

Additionally, long-term stability is also a critical factor to evaluate good ORR material. So, the amperometric i-t curve tests were further applied to explore the durability of the PtP_2@PNC. The chronoamperometric measurement results of PtP_2@PNC and commercial Pt/C are depicted in Figure 5F. After 24-h *i–t* test, the current of PtP_2@PNC exhibits a slight decrease (~8%). Nevertheless, the current of Pt/C shifts negatively by about ~14% after only 3-h test, suggesting the current loss of PtP_2@PNC is much smaller than the commercial Pt/C. Such excellent stability of PtP_2@PNC can be mainly attributed to the improved phosphorus and nitrogen-doped carbon structure (Pu et al., 2017; Qin et al., 2018, 2019). Additionally, the robust PNC layers could confine the PtP_2 NPs and prevent the PtP_2 active centers from aggregation. The morphology data of PtP_2@PNC catalyst after the stability test were characterized by TEM. As shown in Figures S28 and S29, TEM suggests that negligible change has been observed for the morphology of catalysts after HOR and ORR stability test, which further demonstrates that the catalyst has good durability.

It is noteworthy that Figures 5G–5I and S30–S32 present the ORR polarization curves of Pt/C and PtP_2@PNC materials in O_2-saturated 0.1 M $HClO_4$ electrolytes. The PtP_2@PNC catalyst has similar ECSA to the commercial Pt/C (Figures 5G and S30). Furthermore, PtP_2@PNC shows an ORR onset potential of 0.87 V and $E_{1/2}$ of 0.74 V, which are slightly different from commercial Pt/C (onset potential: 0.94 V; $E_{1/2}$ = 0.85 V) (Figures

5H and S31). Additionally, commercial Pt/C exhibits MA and specific activity of 48.2 mA mg_{Pt}^{-1} and 0.066 mA cm^{-2} at 0.9 V versus RHE, respectively, which are slightly better than that of commercial PtP_2@PNC (17.6 mA mg_{Pt}^{-1} and 0.0 38 mA cm^{-2} at 0.9 V vs. RHE) (Figure 5I). It is worth noting that the ORR path of PtP_2@PNC is nearly four electron transfer path in the acidic electrolytes based on K-L formula (Figure S32).

More importantly, in order to achieve a comparable or even superior ORR activity of $PtP_{2@}$PNC materials to the Pt/C, we increased the PtP_2 content in the compounds by adding the H_2PtCl_6 (~300 mg) precursor during the synthesis process (the obtained materials named as PtP_2@PNC-3, ~24 wt % Pt). As illustrated in Figure S33A, PtP_2@PNC-3 shows a higher ORR activity than that of commercial Pt/C in alkaline solutions. In addition, it further exhibits identical ORR activity compared with the 20 wt % commercial Pt/C in acidic solutions (Figure S33B).

For industrial application in fuel cells, besides superior activity and high durability, a good catalyst should be able to afford the possible methanol (CH_3OH) crossover and carbon monoxide (CO) poisoning, which may significantly harm the performance of the full cell (Zitolo et al., 2015; Dai et al., 2015). Thus, we measured the i-t response of the PtP_2@PNC in the presence of CO and methanol, respectively. As shown in Figure S34A, when introducing 3.0 M methanol into the 0.1 M KOH solutions, the current density of commercial Pt/C instantaneously decreases, indicating the occurrence of methanol oxidation. In contrast, the ORR current density of PtP_2@PNC only shows a slight change, suggesting that PtP_2@PNC possesses better methanol resistance than that of Pt/C. Similarly, PtP_2@PNC has no CO poisoning, whereas Pt/C is fast poisoned with a gradually dropped current density (Figure S34B). These results demonstrate that PtP_2@PNC has much higher ORR activity and selectivity than that of commercial Pt/C and is free from the CH_3OH and CO poisoning, promising for practical applications in fuel cells and other energy-related conversion and storage devices.

Conclusion

In summary, we have achieved high-efficiency PtP_2 materials embedded in PNC layer with a low Pt mass loading (only 3.5 wt %) by a facile solid-state pyrolysis approach under ambient pressure and moderate temperatures. As expected, the obtained PtP_2@PNC catalyst possesses excellent HER activity (8 mV @j = 10 mA cm^{-2}) and durability in acidic solutions. Such high HER activity is superior to not only commercial Pt/C material but also all the reported HER catalysts. For the HOR, its mass activity (MA) at an overpotential of 40 mV is 2.3-fold over that of the commercial Pt/C catalyst. Furthermore, the PtP_2@PNC catalyst exhibits nearly 2.6 times ORR MA than that of 20 wt % commercial Pt/C, as well as greatly improved ORR stability and fuel tolerance than that of Pt/C. The outstanding HER, HOR, and ORR catalytic performances of our PtP_2@PNC catalyst make PtP_2 a promising multifunctional catalyst for wide applications in energy conversion and storage devices.

Limitations of the Study

This study has demonstrated an advanced multifunctional catalyst for hydrogen evolution/oxidation reactions and oxygen reduction reaction from experimental and theoretical perspectives. The experimental results suggested that the catalysts illustrated high HER, HOR, and ORR performance. DFT calculation was also used to investigate the mechanism. However, an in-depth understanding of the catalytic mechanism is still needed by further *in situ* characterizations. As a result, we will keep working on development and perfection on related mechanism exploration based on a series of *in situ* technologies.

Resource Availability

Lead Contact

Further information and requests for resources should be directed to and will be fulfilled by the Lead Contact, Shichun Mu (msc@whut.edu.cn).

Materials Availability

All unique/stable reagents generated in this study are available from the Lead Contact without restriction.

Data and Code Availability

All data used in the study are included in this publication. The present research did not use any new codes.

METHODS

All methods can be found in the accompanying Transparent Methods supplemental file.

SUPPLEMENTAL INFORMATION

Supplemental Information can be found online at https://doi.org/10.1016/j.isci.2020.101793.

ACKNOWLEDGMENTS

This work was supported by the National Natural Science Foundation of China (51672204, 22075223). We express heartfelt thanks to Prof. Gaoke Zhang for the supply of computational resources in the School of Resources and Environmental Engineering, Wuhan University of Technology. The authors also wish to sincerely acknowledge the anonymous reviewers for their constructive engagement, prompt feedback, and valuable suggestions.

AUTHOR CONTRIBUTIONS

Z.P. and S.M. designed the studies. Z.P., R.C., J.Z., P.W., I.S.A., Z.W., D.C., and M.W. conducted the synthesis, characterization, and catalytic tests of the catalysts. Z.H. and C.L. conducted HRTEM characterization. W.L. performed the DFT calculations. Z.P. and S.M. wrote the manuscript. All authors discussed the results and commented on the manuscript.

DECLARATION OF INTERESTS

The authors declare no competing interests.

Received: August 28, 2020
Revised: October 21, 2020
Accepted: November 6, 2020
Published: December 18, 2020

REFERENCES

Amiinu, I.S., Pu, Z., Liu, X., Owusu, K.A., Monestel, H.G.R., Boakye, F.O., Zhang, H., and Mu, S. (2017). Multifunctional Mo–N/C@MoS_2 electrocatalysts for HER, OER, ORR, and Zn–Air batteries. Adv. Funct. Mater. *27*, 1702300.

Andronescu, C., Barwe, S., Ventosa, E., Masa, J., Vasile, E., Konkena, B., Möller, S., and Schuhmann, W. (2017). Powder catalyst fixation for post-electrolysis structural characterization of NiFe layered double hydroxide based oxygen evolution reaction electrocatalysts. Angew. Chem. Int. Ed. *56*, 11258–11262.

Balat, M., and Balat, H. (2009). Biogas as a renewable energy source-a review. Energy Source A *31*, 1280–1293.

Bu, L., Shao, Q., Bin, E., Guo, J., Yao, J., and Huang, X. (2017). PtPb/PtNi intermetallic core/atomic layer shell octahedra for efficient oxygen reduction electrocatalysis. J. Am. Chem. Soc. *139*, 9576–9582.

Cui, Z., Chen, H., Zhao, M.E., Marshall, D., Yu, Y., Abruna, H., and DiSalvo, F.J. (2014). Synthesis of structurally ordered Pt_3Ti and Pt_3V nanoparticles as methanol oxidation catalysts. J. Am. Chem. Soc. *136*, 10206–10209.

Cui, Z., Chen, H., Zhou, W., Zhao, M., and DiSalvo, F.J. (2015a). Structurally ordered Pt_3Cr as oxygen reduction electrocatalyst: ordering control and origin of enhanced stability. Chem. Mater. *27*, 7538–7545.

Cui, W., Liu, Q., Xing, Z., Asiri, A.M., Alamry, K.A., and Sun, X. (2015b). MoP nanosheets supported on biomass-derived carbon flake: one-step facile preparation and application as a novel high-active electrocatalyst toward hydrogen evolution reaction. Appl. Catal. B Environ. *164*, 144–150.

Dai, L., Xue, Y., Qu, L., Choi, H.J., and Baek, J.B. (2015). Metal-free catalysts for oxygen reduction reaction. Chem. Rev. *115*, 4823–4892.

Dubau, L., Durst, J., Maillard, F., Guetaz, L., Chatenet, M., Andre, J., and Rossinot, E. (2011). Further insights into the durability of Pt_3Co/C electrocatalysts: formation of "hollow" Pt nanoparticles induced by the Kirkendall effect. Electrochm. Acta *56*, 10658–10667.

Fan, Z., and Zhang, H. (2016). Crystal phase-controlled synthesis, properties and applications of noble metal nanomaterials. Chem. Soc. Rev. *45*, 63–82.

Greeley, J., Stephens, I.E.L., Bondarenko, A.S., Johansson, T.P., Hansen, H.A., Jaramillo, T.F., Rossmeisl, J., Chorkendorff, I., and Nørskov, J.K. (2009). Alloys of platinum and early transition metals as oxygen reduction electrocatalysts. Nat. Chem. *1*, 552–556.

Guo, Y., Yuan, P., Zhang, J., Xia, H., Cheng, F., Zhou, M., Li, J., Qiao, Y., Mu, S., and Xu, Q. (2018). Co_2P–CoN double active centers confined in N-doped carbon nanotube: heterostructural engineering for trifunctional catalysis toward HER, ORR, OER, and Zn–air batteries driven water splitting. Adv. Funct. Mater. 1805641.

Huang, X., Zhao, Z., Cao, L., Chen, Y., Zhu, E., Lin, Z., Li, M., Yan, A., Zettl, A., Wang, Y.M., et al. (2015). High-performance transition metal–doped Pt_3Ni octahedra for oxygen reduction reaction. Science *348*, 1230–1234.

Huang, R., Sun, Z., Chen, S., Wu, S., Shen, Z., Wu, X., and Zeng, J. (2017). Pt–Cu hierarchical quasi great dodecahedrons with abundant twinning defects for hydrogen evolution. Chem. Commun. *53*, 6922–6995.

Hunt, S.T., Milina, M., Alba-Rubio, A.C., Hendon, C.H., Dumesic, J.A., and Román-Leshkov, Y. (2016). Self-assembly of noble metal monolayers on transition metal carbide nanoparticle catalysts. Science *352*, 974–978.

Kalinkin, A.V., Smirnov, M.Y., Nizovskii, A.I., and Bukhtiyarov, V.I. (2010). X-ray photoelectron spectra of platinum compounds excited with monochromatic AgLα irradiation. J. Electron Spectrosc. *177*, 15–18.

Kibsgaard, J., Jaramillo, T.F., and Besenbacher, F. (2014). Building an appropriate active-site motif into a hydrogen-evolution catalyst with thiomolybdate $[Mo_3S_{13}]^{2-}$ clusters. Nat. Chem. *6*, 248–253.

Lee, J.S., Kim, S.T., Cao, R., Choi, N.S., Liu, M., Lee, K.T., and Cho, J. (2011). Metal–air batteries with high energy density: Li–air versus Zn–air. Adv. Energy Mater. *1*, 34–50.

Li, W., Amiinu, I.S., Ye, B., Wang, Z., Zhu, J., Kou, Z., and Mu, S. (2018). TePtFe nanotubes as high-performing bifunctional electrocatalysts for the oxygen reduction reaction and hydrogen evolution reaction. Chem. Sus. Chem. *11*, 1328–1333.

Liu, Q., Tian, J., Cui, W., Cheng, N., Asiri, A.M., and Sun, X. (2014). Carbon nanotubes decorated with CoP nanocrystals: a highly active non-noble-metal nanohybrid electrocatalyst for hydrogen evolution. Angew. Chem. Int. Ed. *53*, 6710–6714.

Luo, F., Zhang, Q., Yu, X., Xiao, S., Ling, Y., Hu, H., Guo, L., Yang, Z., Huang, L., Cai, W., and Cheng, H. (2018). Palladium phosphide as a stable and efficient electrocatalyst for overall water splitting. Angew. Chem. Int. Ed. *57*, 14862–14867.

Ma, T.Y., Ran, J.R., Dai, S., Jaroniec, M., and Qiao, S.Z. (2015). Phosphorus-Doped graphitic carbon nitrides in situ grown on carbon fiber paper: flexible and reversible oxygen electrodes. Angew. Chem. Int. Ed. *54*, 4646–4650.

Ma, Z., Cano, Z.P., Yu, A., Chen, Z., Jiang, G., Fu, X., and Lu, J. (2020a). Enhancing Oxygen reduction activity of Pt-based electrocatalysts: from theoretical mechanisms to practical methods. Angew. Chem. Int. Ed. *59*, 18334–18348.

Ma, Z., Li, S., Wu, L., Song, L., Jiang, G., Liang, Z., Su, D., Zhu, Y., Adzic, R., Wang, J., and Chen, Z. (2020b). NbO_x nano-nail with a Pt head embedded in carbon as a highly active and durable oxygen reduction catalyst. Nano Energy *69*, 104455.

Mallouk, T.E. (2013). Water electrolysis: divide and conquer. Nat. Chem. *5*, 362–363.

Morales-Guio, C.G., Stern, L.A., and Hu, X. (2014). Nanostructured hydrotreating catalysts for electrochemical hydrogen evolution. Chem. Soc. Rev. *43*, 6555–6569.

Popczun, E.J., McKone, J.R., Read, C.G., Biacchi, A.J., Wiltrout, A.M., Lewis, N.S., and Schaak, R.E. (2013). Nanostructured nickel phosphide as an electrocatalyst for the hydrogen evolution reaction. J. Am. Chem. Soc. *135*, 9267–9270.

Porter, N.S., Wu, H., Quan, Z.W., and Fang, J.Y. (2013). Shape-control and electrocatalytic activity-enhancement of Pt-based bimetallic nanocrystals. Acc. Chem. Res. *46*, 1867–1877.

Pu, Z., Amiinu, I.S., Kou, Z., Li, W., and Mu, S. (2017). RuP_2-based catalysts with platinum-like activity and higher durability for the hydrogen evolution reaction at all pH values. Angew. Chem. Int. Ed. *56*, 11559–11564.

Qin, Q., Jang, H., Chen, L., Nam, G., Liu, X., and Cho, J. (2018). Low loading of Rh_xP and RuP on N, P codoped carbon as two trifunctional electrocatalysts for the oxygen and hydrogen electrode reactions. Adv. Energy Mater. *8*, 1801478.

Qin, Q., Jang, H., Chen, L., Li, P., Wei, T., Liu, X., and Cho, J. (2019). Coupling a low loading of IrP_2, PtP_2, or Pd_3P with heteroatom-doped nanocarbon for overall water-splitting cells and zinc–air batteries. ACS Appl. Mater. Interfaces *11*, 16461–16473.

Robinson, J.T., Pietron, J.J., Blue, B., Perkins, F.K., Josberger, E., Deng, Y., and Rolandi, M. (2017). Electrical and electrochemical characterization of proton transfer at the interface between chitosan and PdH_x. J. Mater. Chem. C *5*, 11083–11091.

Shan, J., Ling, T., Davey, K., Zheng, Y., and Qiao, S. (2019). Transition-metal-doped RuIr bifunctional nanocrystals for overall water splitting in acidic environments. Adv. Mater. *31*, 1900510.

Shi, Y., and Zhang, B. (2016). Recent advances in transition metal phosphide nanomaterials: synthesis and applications in hydrogen evolution reaction. Chem. Soc. Rev. *45*, 1529–1541.

Steele, B.C., and Heinzel, A. (2001). Materials for fuel-cell technologies. Nature *414*, 345–352.

Tian, X., Lu, X., Xia, B., and Lou, X. (2020a). Advanced electrocatalysts for the oxygen reduction reaction in energy conversion technologies. Joule *4*, 45–68.

Tian, W., Wang, Y., Fu, W., Su, J., Zhang, H., and Wang, Y. (2020b). PtP_2 nanoparticles on N, P doped carbon through a self-conversion process to core–shell Pt/PtP_2 as an efficient and robust ORR catalyst. J. Mater. Chem. A. *8*, 20463–20473.

Turner, J.A. (2004). Sustainable hydrogen production. Science *305*, 972–974.

Wang, C., Vliet, D.V.D., More, K.L., Zaluzec, N.J., Peng, S., Sun, S., Daimon, H., Wang, G., Greeley, J., and Pearson, J. (2011). Multimetallic $Au/FePt_3$ nanoparticles as highly durable electrocatalyst. Nano Lett. *11*, 919–926.

Wang, S., Zhang, L., Xia, Z., Roy, A., Chang, D.W., Baek, J.B., and Dai, L. (2012). BCN graphene as efficient metal-free electrocatalyst for the oxygen reduction reaction. Angew. Chem. Int. Ed. *124*, 4285–4288.

Wang, X., Choi, S.I., Roling, L.T., Luo, M., Ma, C., Zhang, L., Chi, M., Liu, J., Xie, Z., Herron, J.A., et al. (2015). Palladium–platinum core-shell icosahedra with substantially enhanced activity and durability towards oxygen reduction. Nat. Commun. *6*, 7594–7602.

Wang, P., Zhang, X., Zhang, J., Wan, S., Guo, S., Lu, G., Yao, J., and Huang, X. (2017). Precise tuning in platinum-nickel/nickel sulfide interface nanowires for synergistic hydrogen evolution catalysis. Nat. Commun. *8*, 14580.

Wang, P., Shao, Q., and Huang, X. (2018a). Updating Pt-based electrocatalysts for practical fuel cells. Joule *2*, 2514–2516.

Wang, J., Yu, L., Hu, L., Chen, G., Xin, H., and Feng, X. (2018b). Ambient ammonia synthesis via palladium-catalyzed electrohydrogenation of dinitrogen at low overpotential. Nat. Commun. *9*, 1795.

Wang, T., Wang, M., Yang, H., Xu, M., Zuo, C., Feng, K., Xie, M., Deng, J., Zhong, J., Zhou, W., et al. (2019). Weakening hydrogen adsorption on nickel via interstitial nitrogen doping promotes bifunctional hydrogen electrocatalysis in alkaline solution. Energy Environ. Sci. *12*, 3522–3529.

Wu, J.B., and Yang, H. (2013). Platinum-based oxygen reduction electrocatalysts. Acc. Chem. Res. *46*, 1848–1857.

Yang, F., Zhao, Y., Du, Y., Chen, Y., Cheng, G., Chen, S., and Luo, W. (2018). A monodisperse Rh_2P-based electrocatalyst for highly efficient and pH-universal hydrogen evolution reaction. Adv. Energy Mater. *8*, 1703489.

Zhang, J., Zhao, Z., Xia, Z., and Dai, L. (2015). A metal-free bifunctional electrocatalyst for oxygen reduction and oxygen evolution reactions. Nat. Nanotechnology *10*, 444–452.

Zhang, J., Qu, L., Shi, G., Liu, J., Chen, J., and Dai, L. (2016a). N, P-codoped carbon networks as efficient metal-free bifunctional catalysts for oxygen reduction and hydrogen evolution reactions. Angew. Chem. Int. Ed. *55*, 2230–2234.

Zhang, J., Qu, L., Shi, G., Liu, J., Chen, J., and Dai, L. (2016b). N,P-codoped carbon networks as efficient metal-free bifunctional catalysts for oxygen reduction and hydrogen evolution reactions. Angew. Chem. Int. Ed. *128*, 2270–2274.

Zhao, Y., Nakamura, R., Kamiya, K., Nakanishi, S., and Hashimoto, K. (2013). Nitrogen-doped carbon nanomaterials as non-metal electrocatalysts for water oxidation. Nat. Commun. *4*, 2390.

Zheng, Y., Jiao, Y., Jaroniec, M., and Qiao, S.Z. (2014a). Advancing the electrochemistry of the hydrogen-evolution reaction through combining experiment and theory. Angew. Chem. Int. Ed. *53*, 2–16.

Zheng, Y., Jiao, Y., Li, L., Xing, T., Chen, Y., Jaroniec, M., and Qiao, S. (2014b). Toward design of synergistically active carbon-based catalysts for electrocatalytic hydrogen evolution. ACS Nano *8*, 5290–5296.

Zheng, Y., Jiao, Y., Zhu, Y., Li, L., Han, Y., Chen, Y., Jaroniec, M., and Qiao, S. (2016). High electrocatalytic hydrogen evolution activity of an anomalous ruthenium catalyst. J. Am. Chem. Soc. *138*, 16174–16181.

Zhou, Z., Fan, T., Yan, Y., Zhang, S., Zhou, Y., Deng, H., Cai, X., Xiao, J., Song, D., Zhang, Q., and Cheng, Y. (2019). One stone with two birds: phytic acid-capped platinum nanoparticles for targeted combination therapy of bone tumors. Biomaterials *194*, 130–138.

Zhu, Y.P., Jing, Y., Vasileff, A., Heine, T., and Qiao, S. (2017). Three-dimensional synergistically active carbon nanofibers for improved oxygen evolution. Adv. Energy Mater. *7*, 1602928.

Zhuang, M., Ou, X., Dou, Y., Zhang, L., Zhang, Q., Wu, R., Ding, Y., Shao, M., and Luo, Z. (2016). Polymer-embedded fabrication of Co_2P nanoparticles encapsulated in N,P-doped graphene for hydrogen generation. Nano Lett. *16*, 4691–4698.

Zitolo, A., Goellner, V., Armel, V., Sougrati, M.T., Mineva, T., Stievano, L., Fonda, E., and Jaouen, F. (2015). Identification of catalytic sites for oxygen reduction in iron-and nitrogen-doped graphene materials. Nat. Mater. *14*, 937–942.

iScience, Volume *23*

Supplemental Information

Anion-Modulated Platinum for High-Performance Multifunctional Electrocatalysis toward HER, HOR, and ORR

Zonghua Pu, Ruilin Cheng, Jiahuan Zhao, Zhiyi Hu, Chaofan Li, Wenqiang Li, Pengyan Wang, Ibrahim Saana Amiinu, Zhe Wang, Min Wang, Ding Chen, and Shichun Mu

Supplemental Information

Transparent Methods

Materials and reagent: All the chemicals reagents were purchased from Sigma-Aldrich (AR grade) and were used as received without further purification. KOH and H_2SO_4, H_2PtCl_6, dicyandiamide, phytic acid (PA), Pt/C (20 wt%), and Nafion (5 wt%) were purchased from Sigma-Aldrich. Deionized water was used in all experiments obtained from an ultra-pure purifier (Ulupure, China, resistivity ≥ 18.2 MΩ).

Synthesis of PtP_2@PNC: Typically, PA (4.0 g), H_2PtCl_6 (0.1g), and dicyandiamide (5.0 g) were dissolved in 100 mL water under stirring, and then the mixture was transferred to a culture dish and dried at 80 °C for 24 h forming a homogeneous powder. After that, the homogeneous powder was transferred into a quartz tube and heated to 900 °C for 2h with a ramp of 5 °C min^{-1} under Ar atmosphere. The obtained products were washed by centrifugation with alcohol and water several times to remove the residue of reactants and finally dried in vacuum at 80 °C. Lastly, the sample of PtP_2@PNC was obtained. For comparison, the PNCsample was also obtained according to the same preparation strategy without introducing H_2PtCl_6.

Preparation of Pt-PNC: The Pt-PNC sample was prepared according to the same preparation strategy of PtP_2@PNC by only using H_2PtCl_6 and PNC as precursor.

Electrochemical ORR measurements: Electrochemical experiments were conducted on a CHI760E electrochemical workstation (CH Instrument Co., USA). Cyclic voltammetry (CV)and rotating disk electrode (RDE) measurements (PineResearch Instrument, USA) were conducted using a standard three-electrode system. All the measurements were carried out at room temperature. Before preparing the catalyst ink, the glassy carbon electrode was finely polished by buckskin and Al_2O_3 powder (50 nm in diameter), repeatedly rinsed in absolute ethanol in advance. The catalyst ink was prepared by dispersing 3 mg catalyst in 1 mL mixed solution of isopropyl alcohol and water (volume ratio 7:3) and 20 μL 5 wt% Nafion solutions. The mixed solutions were disposed for 15 min by ultrasonic cell disruptor, and then 10 μL homogeneous catalyst ink was deposited on the glassy carbon electrode, the electrode was allowed to dry at room temperature for 15 min to form a smooth catalyst ring. Commercial Pt/C was prepared in the same way applied to the PtP_2@PNC. A typical three-electrode system was employed, using a glass carbon RDE covered by catalystas working electrode, a platinum wire as the counter electrode, and a SCE as a reference electrode. All potentials in this study were converted to potential vs. reversible hydrogen electrode (RHE). As for ORR experiment, O_2 was bubbled for 20 min prior to the test and maintained in the headspace of the electrolyte throughout the testing process. The working electrode was scanned cathodically at a rate of 5 mV s^{-1} with varying rotating speed from 400 to 2250 rpm in O_2-saturated 0.1 M KOH aqueous solution. The electron transfer number per oxygen molecule for oxygen reduction can be determined on the basis of the Koutechy-Levich equations:

$$\frac{1}{J} = \frac{1}{J_l} + \frac{1}{J_k} = \frac{1}{J_k} + \frac{1}{B\omega^{\frac{1}{2}}} \quad (1)$$

$$B = 0.62nFC_0 \mathrm{D}_0^{\frac{2}{3}} \mathrm{v}^{\frac{-1}{6}} \quad (2)$$

$$J_k = nFkxC_0 \quad (3)$$

Where J is the measured current density and ω is the electrode rotating rate (rad s^{-1}). B is determined from the slope of the Koutechy-Levich (K-L) plot based on Levich equation (2). J_L and J_K are the diffusion and kinetic-limiting current densities, n is the transferred electron number, F is the Faraday constant (F= 96485 C mol^{-1}), C_0 is the O_2 concentration in the electrolyte ($C_0 = 1.26 \times 10^{-6}$ mol cm^{-3}), D_0 is the diffusion coefficient of O_2 ($D_0 = 1.93 \times 10^{-5}$ cm^2 s^{-1}), and v is the kinetic viscosity (v = 0.01009 cm^2 s^{-1}). The constant 0.62 is adopted when the rotation speed is expressed in rad s^{-1}. For ORR experiments, theLSV curves were obtained at a scan rate of 5 mV s^{-1}. To obtain astable current, the LSV data were collected at the second sweep.

HER and HOR measurement: The HER and HOR electrochemical measurements were conducted in a typical three-electrode setup with an electrolyte solution of 0.5 M H_2SO_4, and 0.1 M $HClO_4$, respectively. The graphite rod and SCE were used as the counter and reference electrode, respectively. Linear sweep voltammograms (LSVs) measurements were conducted in 0.5 M H_2SO_4, and 0.1 M $HClO_4$ with a scan rate of 5 mV s^{-1}. The polarization curves were observed by the formula: $E_{actual}= E_{test}- iR\times100\%$. Catalyst ink was prepared by dispersing 5 mg of catalyst into 1 mL of water/ethanol (v/v=1:1) solvent containing 20 μL of 5 wt% Nafion. Then the mixture was ultrasonically suspended for 30 min. 20 and 10 μL of this catalyst ink was dropped on the glassy carbon electrode for HER and HOR tests, respectively. The PtP_2@PNC loading is 0.51 and 0.255 mg cm^{-2} for HER and HOR measurements, respectively. Commercial Pt/C was prepared in the same way applied to the PtP_2@PNC.

ICP-AES measurement: Inductively coupled plasma atom emission spectrometry (ICP-AES) analysis was performed on Optima Prodigy 7 (LEEMAN LABS Ltd., USA). The ICP-AES elemental analyses were performed to obtain the Pt amount in the PtP_2@PNC. Specifically, 2.0 mg PtP_2@PNC was placed in a 50 mL Teflon-lined autoclave, and 5.0 mL HNO_3, 1.0 mL HCl and 1.0 mL HF were then added. The Teflon-lined autoclave was subsequently sealed and treated at 200℃ for 5 h. After cooling to room temperature, the solution in the Teflon-lined autoclave was diluted with water to 25 mL in a volumetric flask. Using the ICP-AES elemental analyses, the concentration of Pt ions in the solution was measured.

Material characterizations: Surface morphology was observed using JSM 7100Ffield emission scanning electron microscopy (FESEM: Zeiss Ultra Plus) fitted with an energy dispersive spectrum analyzer and operated at 5 kV. Structural features were characterized by transmission electron microscopy (TEM) on a JEM 2010 FEF microscope operated at 200 kV. Aberration-corrected High-angle annular dark-field scanning transmission electron microscopy (HAADF-STEM) images of samples were recorded on a JEOL JEM-2010 LaB6 high-resolution transmission electron microscope at 200 kV. Powder X-ray diffraction (XRD) patterns were collected on a Rigaku X-ray diffractometer equipped with a Cu Kα radiation source. X-ray photoelectron spectroscopy (XPS) spectra were recorded on a VG MultiLab 2000 spectrometer using Mg as the exciting source. Raman spectra were obtained on J-Y T64000 Raman spectrometer with 514.5 nm wavelength incident laser light.

Rotation disk electrode (RDE) technique: The catalyst coated working electrode was electrochemically scanned at 5 mV s^{-1} at various rotation speed from 400 to 2250 rpm. The Koutecky–Levich (K–L) plots (j^{-1} versus $\omega^{-1/2}$) were evaluated at various potentials, and the best-fit line slopes were used in the calculations.

The number of electrons transferred (n) is calculated from the following equations:

$$\frac{1}{J} = \frac{1}{J_l} + \frac{1}{J_k} = \frac{1}{J_k} + \frac{1}{B\omega^{\frac{1}{2}}} \quad (4)$$

$$B = 0.62nFC_0 D_0^{\frac{2}{3}} v^{\frac{-1}{6}} \quad (5)$$

$$J_k = nFkxC_0 \quad (6)$$

Where J is the measured current density and is the electrode rotating rate (rad s^{-1}). B is determined from the slope of the Koutechy-Levich (K-L) plot based on Levich equation (5). J_L and J_K are the diffusion and kinetic-limiting current densities, n is the transferred electron number, F is the Faraday constant (F= 96485 C mol^{-1}), C_0 is the O_2 concentration in the electrolyte (C_0 = 1.26 × 10^{-6} mol cm^{-3}), D_0 is the diffusion coefficient of O_2 (D_0 = 1.93 × 10^{-5} cm^2 s^{-1}), and v is the kinetic viscosity (v = 0.01009 cm^2 s^{-1}). The constant 0.62 is adopted when the rotation speed is expressed in rad s^{-1}. For ORR experiments, the LSV curves were obtained at a scan rate of 5 mV s^{-1}. In order to obtain a stable current, the LSV data were collected at the second sweep.

DFT Computational Methods

The Plane-wave Density Functional Theory (DFT) calculations were conducted using the CASTEP module (an Ab Initio Total Energy Program) of Materials Studio 8.0 (Code version: 6546), with the hydrogen binding energy calculated from different active sites (Segall et al., 2002). The generalized gradient approximation (GGA) method with a Perdew-Burke-Ernzerhof (PBE) functional was used to treat the electron exchange correlation (EEC) interaction. The band energy and Fermi energy convergence tolerance were set at 1.0 ×10^{-5} and 2.7 ×10^{-5} eV, respectively. The DOS kpoint separation was set at 0.05 $Å^{-1}$. A Monkhorst–Pack grid k-points of 3×1×1 and a plane wave basis set cut-off energy of 300 eV were used for the Brillouin zone integration. The structures were optimized for force and energy convergence set at 2.0×10^{-5} eV and 0.05 eV $Å^{-1}$, respectively. The self-consistence field (SCF) was 2.0×10^{-6} eV/atom. To consider the influence of van der Waals interaction, the semi-empirical DFT-D force-field approach was applied (Kresse, et al., 1999, Grimme et al., 2006). The Gibb's free energies for hydrogen absorption ΔG_{H^*} were calculated from the given equation:

$\Delta G_{H^*} = \Delta E_{H^*} + \Delta ZPE - T\Delta S$

Where the symbols represent the binding energy (ΔE), the change in zero-point energy (ΔE_{ZPE}), Temperature (T), and the entropy change (ΔS) of the system, respectively. The TΔS and ΔZPE are obtained as previously reported by Norskov et al (Nørskov et al., 2005). Thus, we adopted the approximation that the vibrational entropy of hydrogen in the adsorbed state is negligible, in which case $\Delta S_H \approx S_{H^*} - 1/2(S_{H2}) \approx -1/2(S_{H2})$, where S_{H2} is the entropy of H_2(g) at standard conditions, and $TS(_{H2})$ is ~0.41 eV for H_2 at 300 K and 1 atm (Nørskov et al., 2005).

Theoretical models

We build the correlative theoretical model to simulate the PtP_2@PNC. The PtP_2@PNC model is constructed by covering the respective PNC layer on the (111) facet of the PtP_2 slab. To minimize the effects of lattice mismatch between the PtP_2 and PNC, we considered an interface periodicity of 2×2 and 4×3 supercells for the PtP_2 and PNC phases of PtP_2@PNC, respectively.

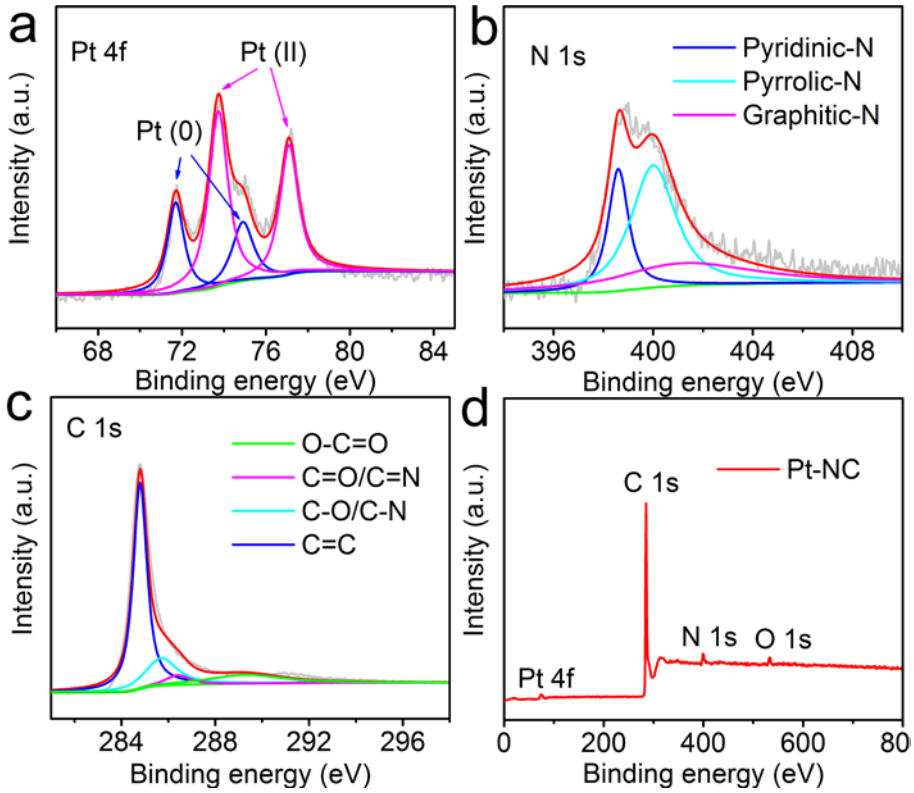

Figure S1. XPS characterization of the obtained Pt-NC, related to Figure 2.

(a-c) High-resolution XPS spectra of the Pt-NC. (d) The survey XPS spectra of the Pt-NC.

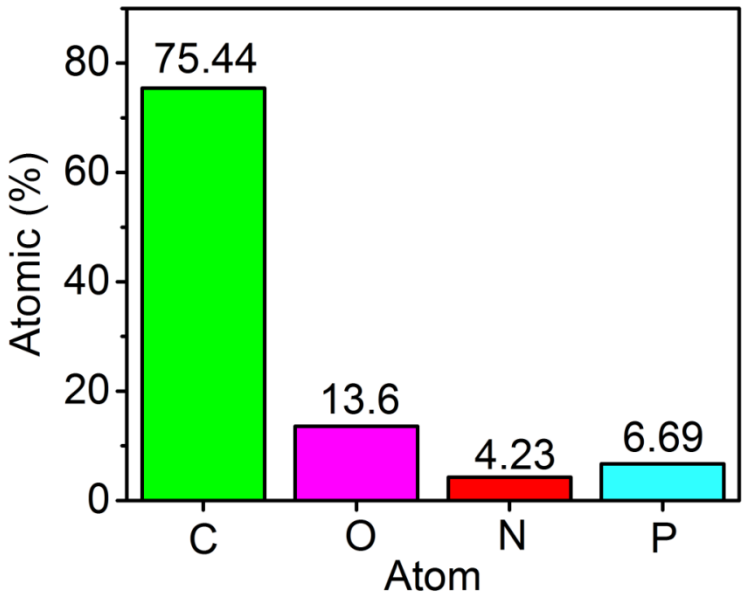

Figure S2.Atomic concentration histogram of synthesized PNC, related to Figure 2.

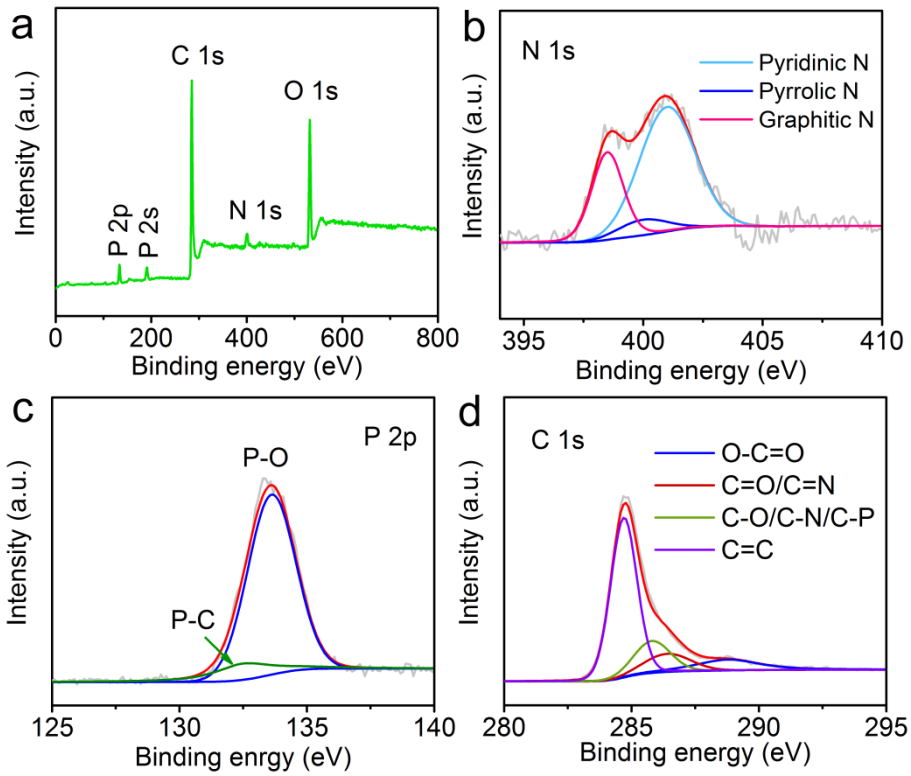

Figure S3. **XPS characterization of the obtained PNC, related to Figure 2.**

(a) XPS spectrum of PNC. (b–d) High-resolution XPS spectra of N 1s, P2p and C 1s, respectively.

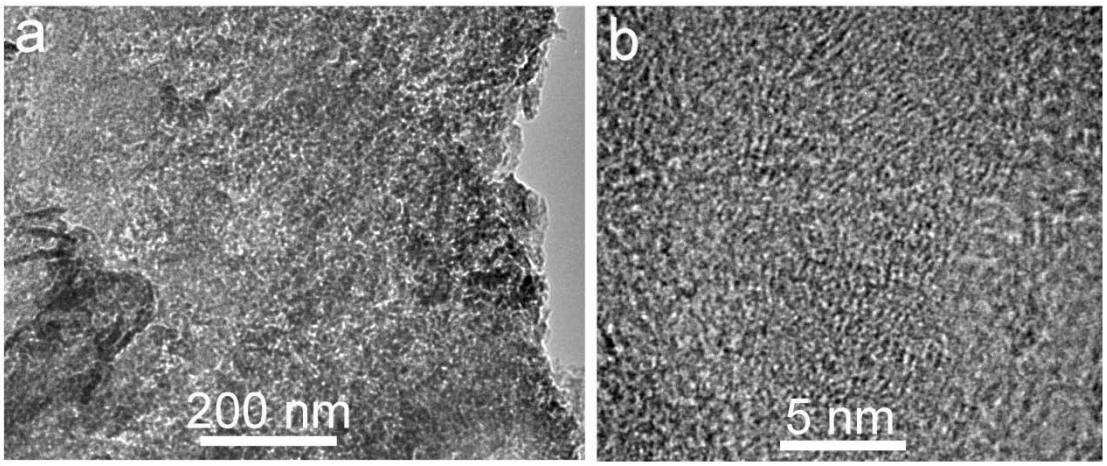

Figure S4. TEM images of PNC layers, related to Figure 2.

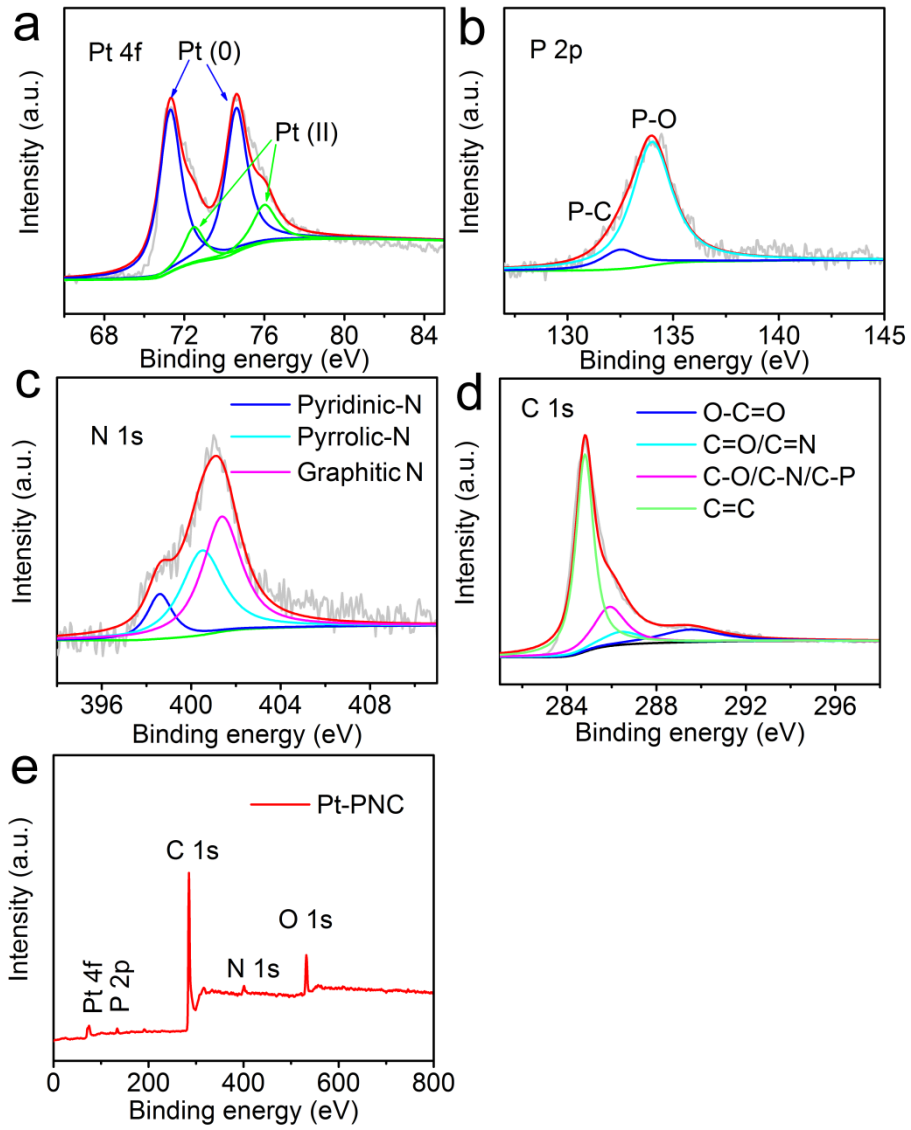

Figure S5. XPS characterization of the obtained Pt-PNC, related to Figure 2.

(a-d) High-resolution XPS spectra of the Pt-PNC. (e) The survey XPS spectra of the Pt-PNC.

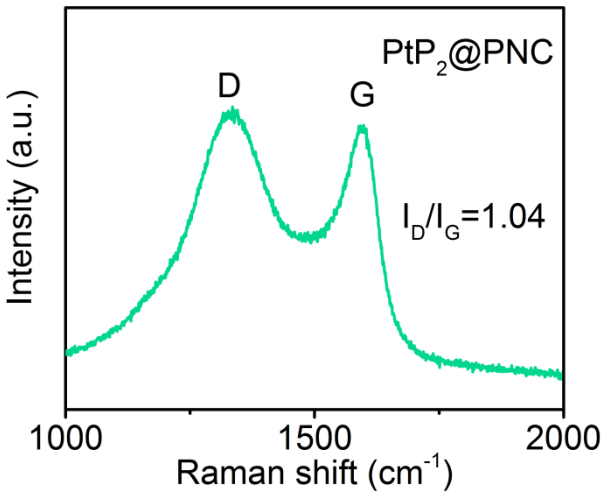

Figure S6. Raman spectrum of PtP_2@PNC, related to Figure 2.

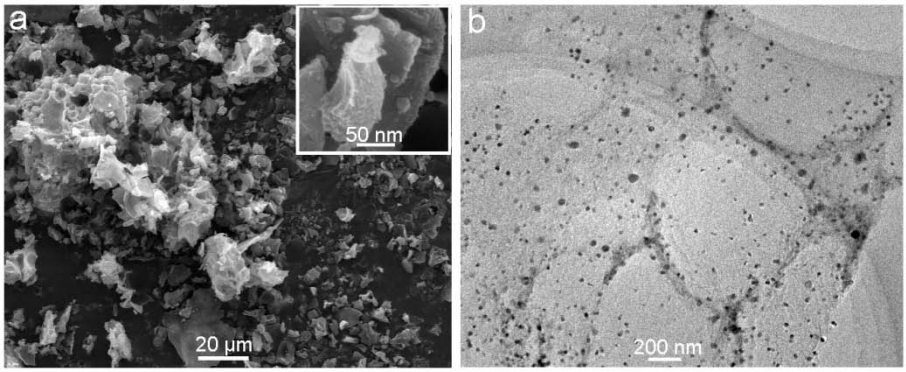

Figure S7. (a) SEM and (b) TEM images of PtP_2@PNC, related to Figure 2.

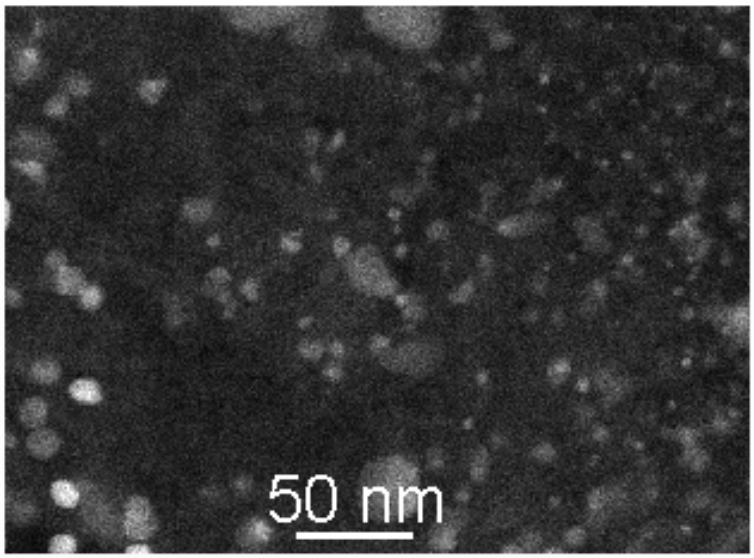

Figure S8. STEM imageof PtP_2@PNC, related to Figure 2.

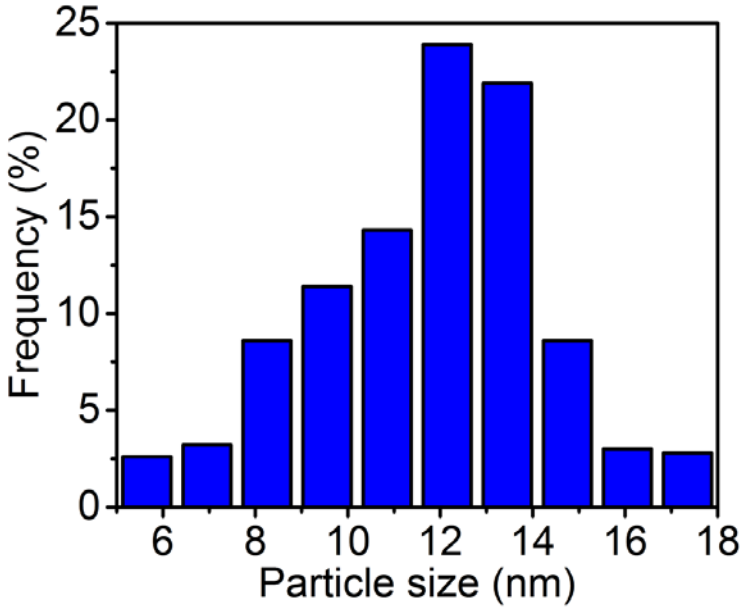

Figure S9. Particle size distribution of PtP_2@PNC, average particle size ≈11.7± 2.5 nm(~100 nanoparticles were measured), related to Figure 2.

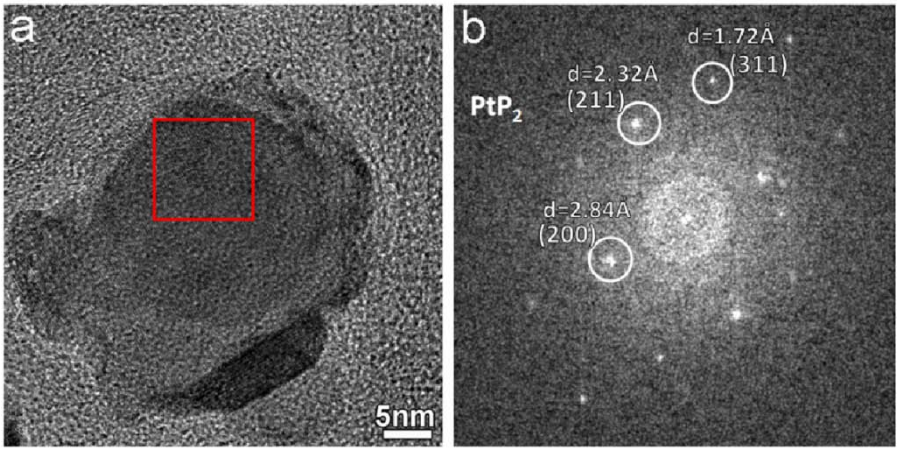

Figure S10. (a) HRTEM image of PtP_2@PNC. (b) Corresponding FFT pattern of the area indicated by the red box in (a), related to Figure 3.

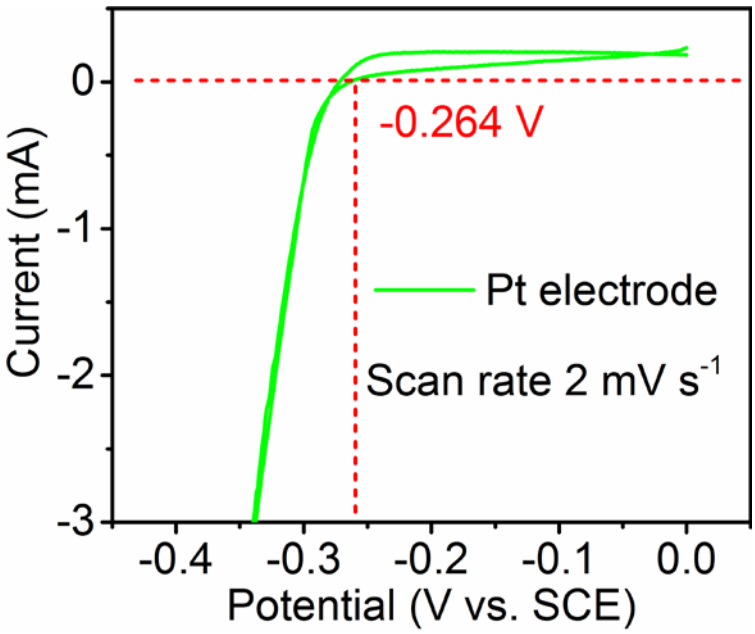

Figure S11. RHE voltage calibration, related to Figure 4.

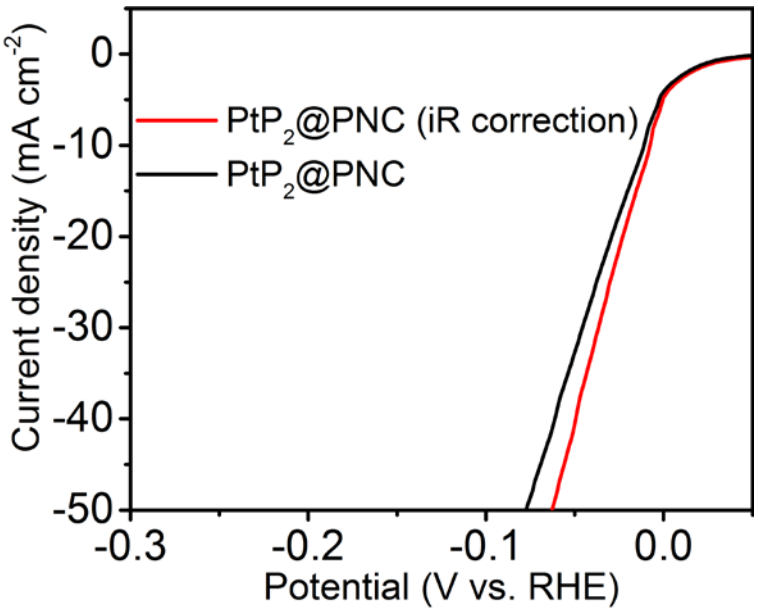

Figure S12. Polarization curves of PtP_2@PNC with/without iR correction, related to Figure 4.

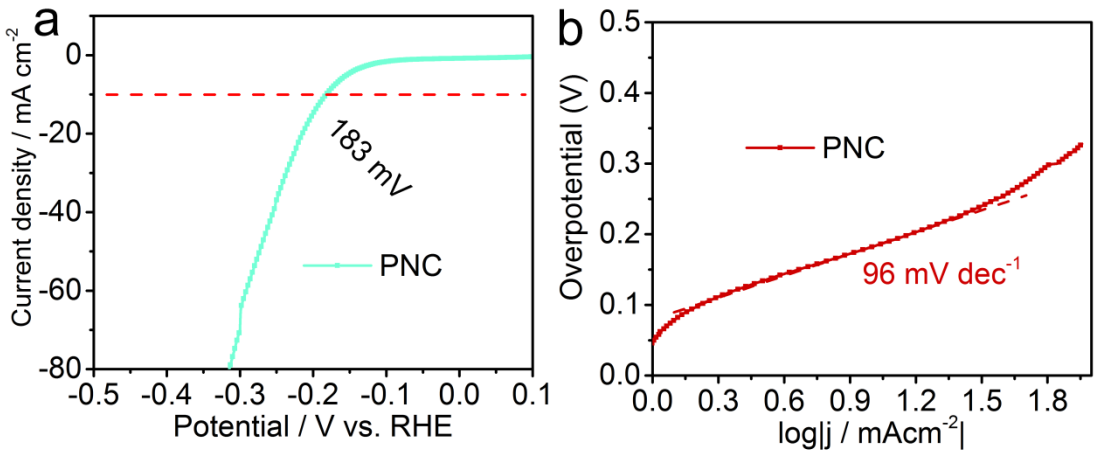

Figure S13. **HER performances of PNC in 0.5 M H_2SO_4 solutions, related to Figure 4.**
(a) HER polarization curve for PNC recorded at 5 mVs^{-1}. (b) Corresponding Tafel slope.

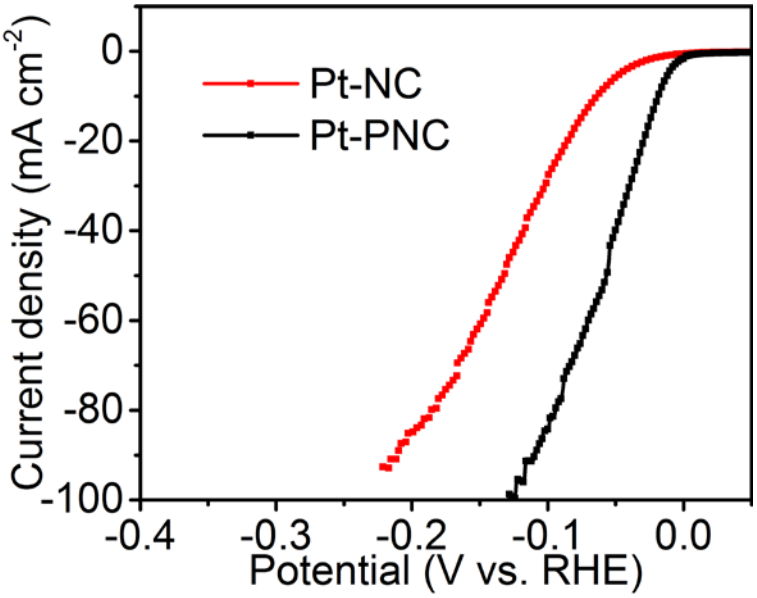

Figure S14. HER activity of Pt-PNC and Pt-NC, related to Figure 4.

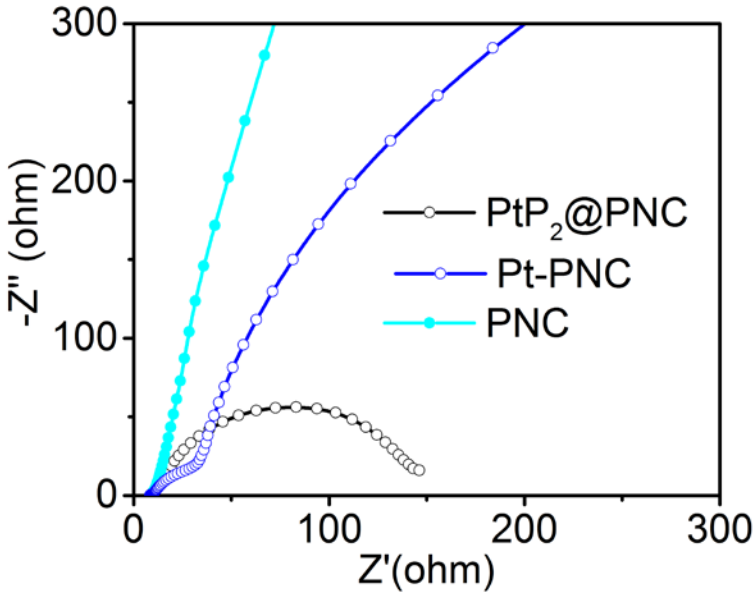

Figure S15. Nyquist plots of PtP_2@PNC, Pt-PNC, and PNC recorded at η=30 mV in 0.5 M H_2SO_4, related to Figure 4.

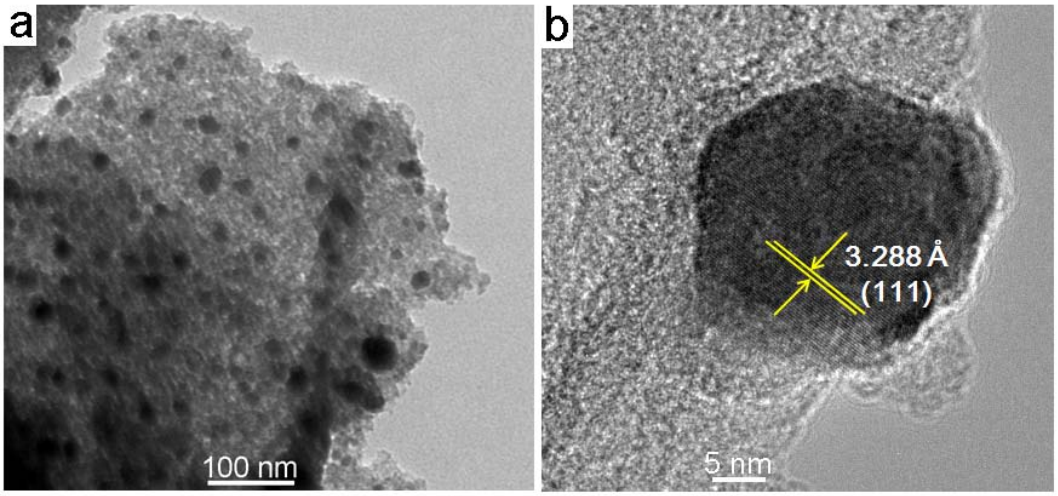

Figure S16. (a) TEM and (b) HRTEM images of post-HER PtP_2@PNC, related to Figure 4.

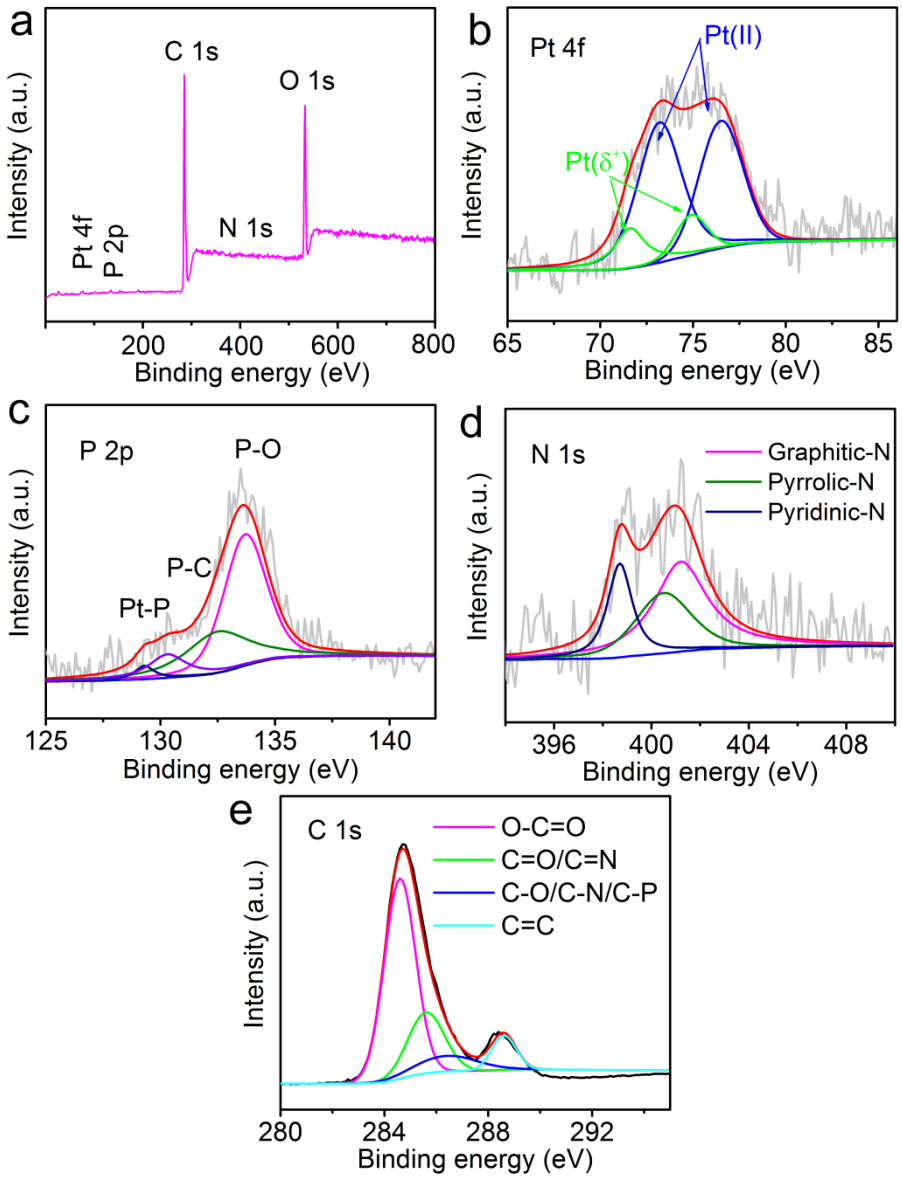

Figure S17. XPS characterizations of post-HER PtP_2@PNC, related to Figure 4.

XPS spectra of (a) survey scan, (b) Pt4f regions, (c) P 2p regions,(d) N 1s regions, and (e) C 1s regions for post-HER PtP_2@PNC.

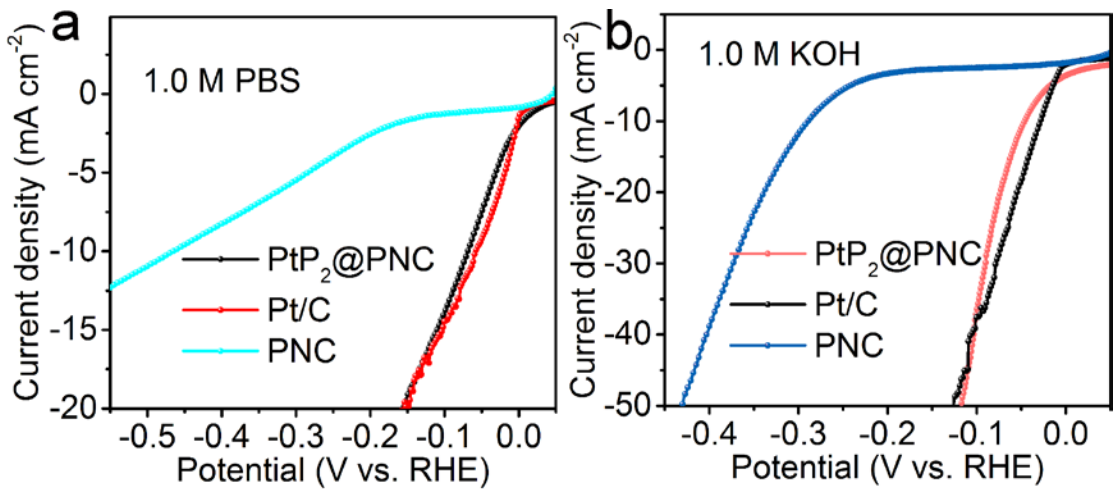

Figure S18. HER performances of PtP_2@PNC, commercial Pt/C and PNC in different environment, related to Figure 4.

HER polarization curves for PtP_2@PNC, commercial Pt/C and PNC under (a) neutral and (b) alkaline solutions.

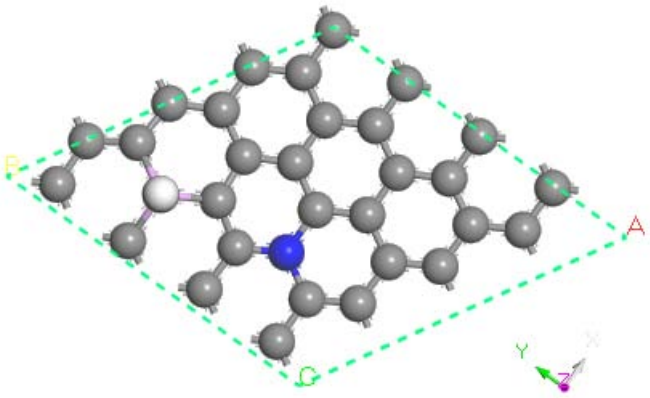

Figure S19. Theoretical model of PNC used in DFT calculations ($\Delta G(H) = 0.57$ eV), related to Figure 4.

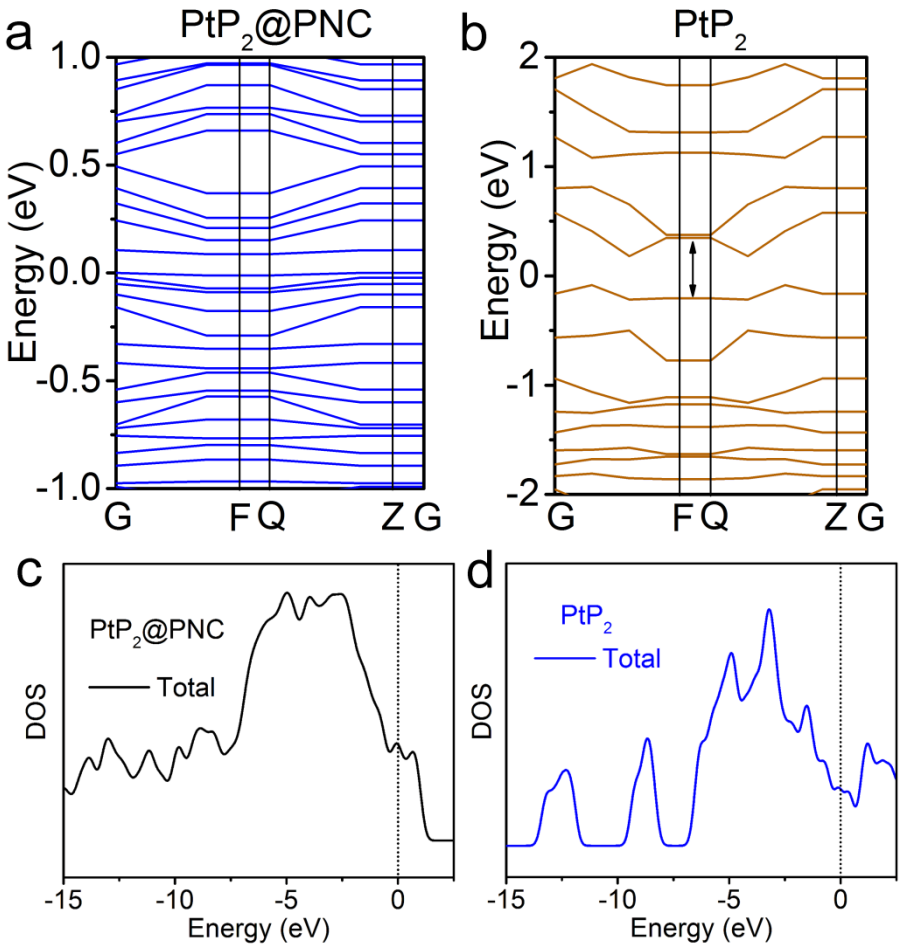

Figure S20. DFT calculations of PtP_2@PNCpure PtP_2, related to Figure 4.
Band structure of (a) PtP_2@PNC and (b) pure PtP_2. Calculated density of states of (c) PtP_2@PNC and (d) PtP_2. The black dotted line represents the Fermi level.

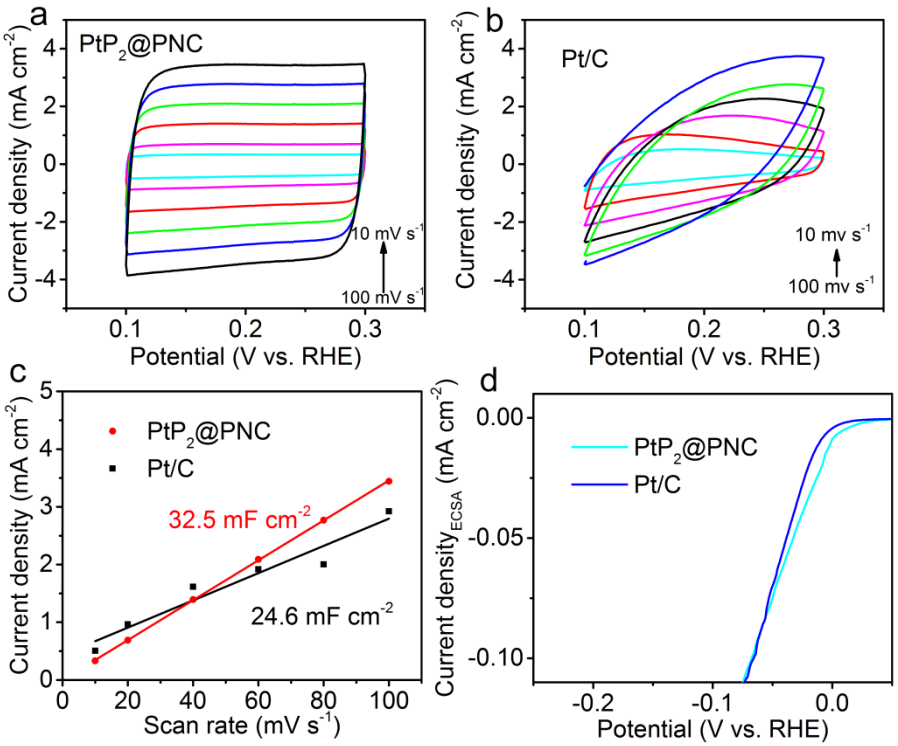

Figure S21. ECSA data of PtP_2@PNC and Pt/C, related to Figure 4.

CV conducted at potential from 0.1 to 0.3 V vs. RHE at scan rates of 10, 20, 40, 60, 80 and 100 mV s^{-1} for (a) PtP_2@PNC and (b) Pt/C. The capacitive currents were measured at 0.2 V vs. RHE. (c) The measured capacitive currents plotted as a function of the scan rate. (d) HER polarization curves of Pt/C and PtP_2@PNC.

The electrochemical active surface area (ECSA) data are obtained based on the electrochemical double-layer capacitance (C_{dl}) through cyclic voltammogram (CV). The linear sweep voltammetry(LSV) curves of Pt/C (20%) and PtP_2@PNC were further plotted by ECSA (**Figure S21d**). In details: CV curves were obtained by cyclic voltammetry from 0.1 to0.3 V vs. RHE, where there was no Faradic current, at scan rate of 10, 20, 40, 60, 80 and 100 mV·s^{-1}. The double-layer capacitance can be calculated as formula, C_{dl} = j/r, where j is the current density and r is the scan rate. ECSA can be calculated as: ECSA=C_{dl}/C_s, where C_s is the specific capacitance value for a flat standard with 1 cm^2 of real surface area. The general value of C_s ranges from 20-60 μF cm^{-2} (Ref: Angew. Chem. Int. Ed. 2014, 53, 14433).In the following calculations of ECSA, 60 μF cm^{-2} is used as C_s.

$ECSA_{PtP2@PNC}$=32.5 mF cm^{-2}/60μF cm^{-2}=541

$ECSA_{Pt/C}$=24.6 mF cm^{-2}/60μF cm^{-2}=410

When the catalytic activity was calculated by the ECSA, thePtP_2@PNC still exhibits higher activity than that of commercial Pt/C. This indicates PtP_2@PNCshows a better intrinsic HER catalytic activity than that of the commercial Pt/C.

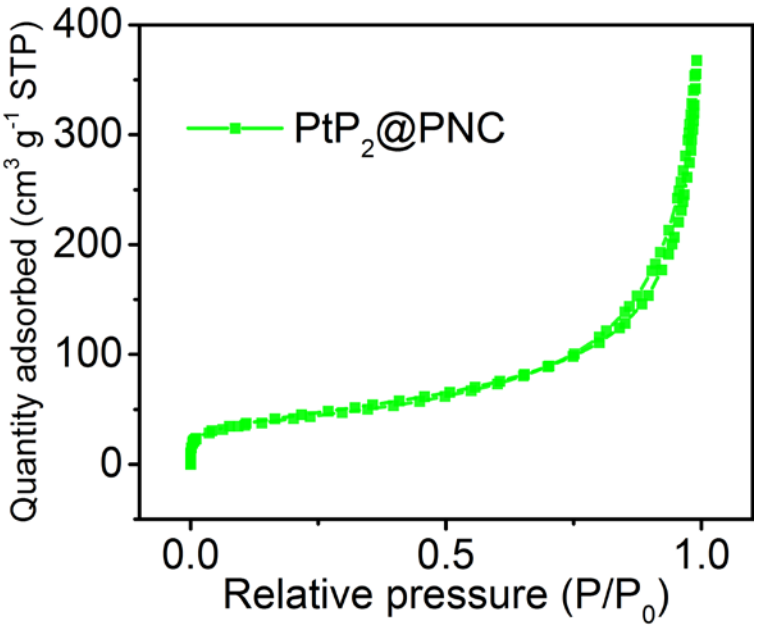

Figure S22. N_2 adsorption and desorption isotherms of PtP_2@PNC, related to Figure 4.

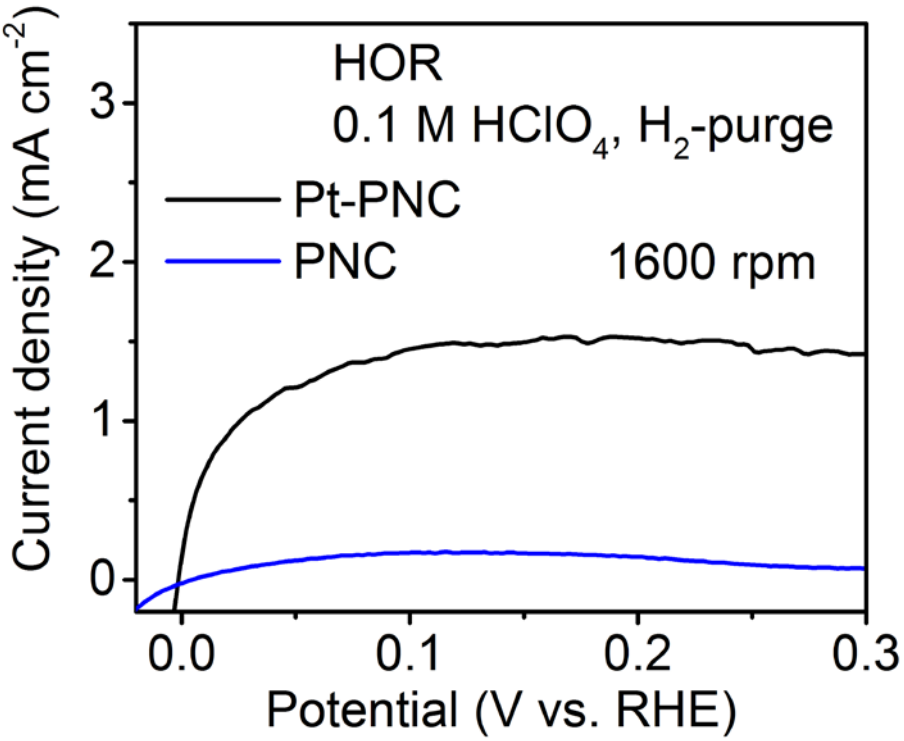

Figure S23. Polarization curves of PNC, and Pt-PNC for HOR in H_2-saturated 0.1 M $HClO_4$, related to Figure 5.

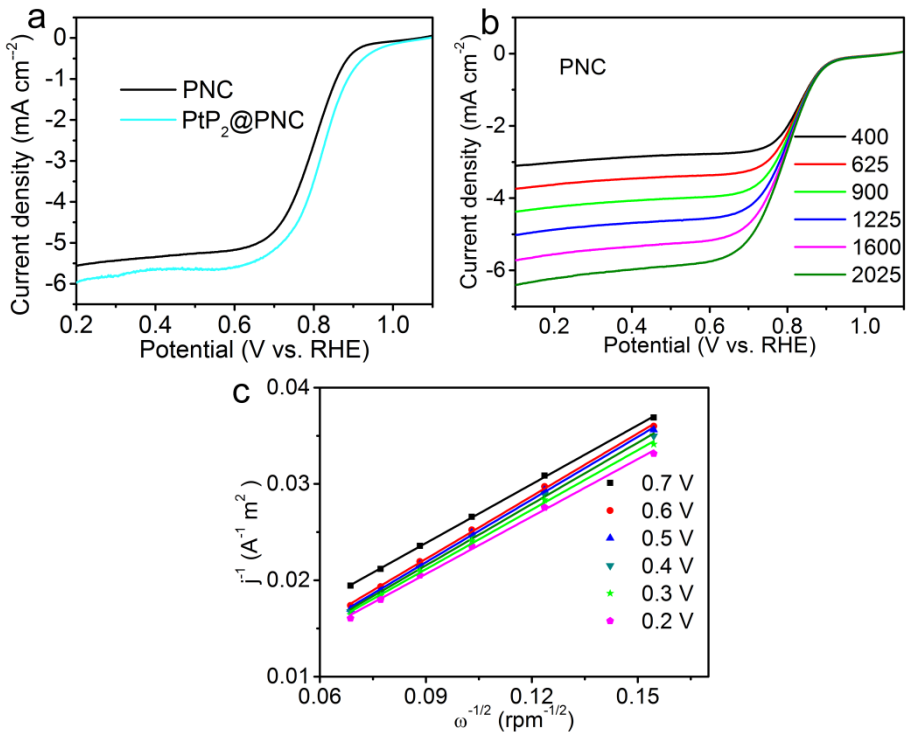

Figure S24. ORR performances of PtP_2@PNC and PNC in alkaline condition, related to Figure 5.

(a) LSV curves of PNC and PtP_2@PNC catalyst at 5 mV s^{-1} at a rotating speed of 1600 rpm obtained in O_2-saturated 0.1 M KOH solutions. (b) LSV curves of PNC at 400, 625, 900, 1225, 1600 and 2025 rpm with a sweep rate of 5 mV s^{-1} in O_2-saturated 0.1 M KOH solutions. (c) K–L plots of PNC at the potential of 0.2, 0.3, 0.4, 0.5, 0.6 and 0.7 V (n = 4.0).

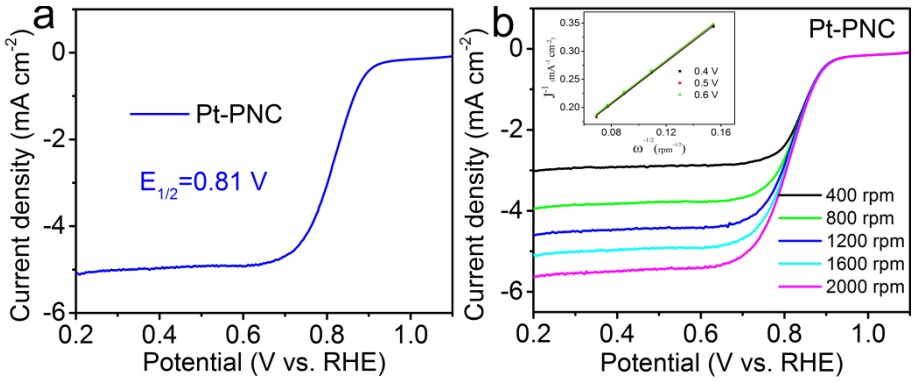

Figure S25. ORR activity for Pt-PNC, related to Figure 5.

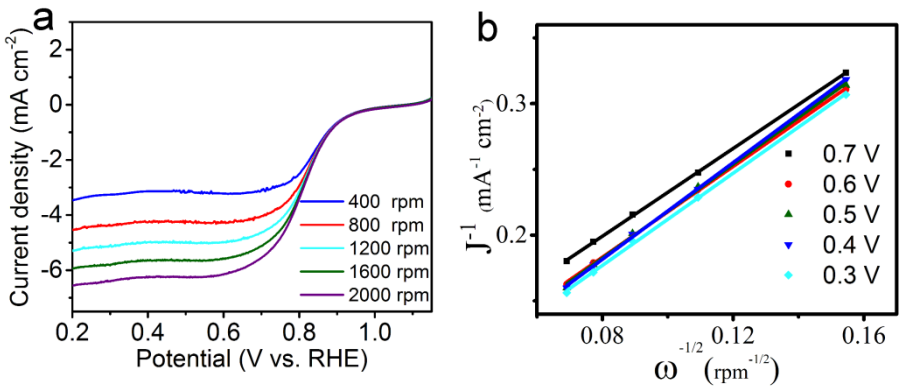

Figure S26. ORR performances of PtP_2@PNC in alkaline condition, related to Figure 5. (a) LSV curves of PtP_2@PNC at different rotation speeds in 0.1 M KOH. (b) The Koutecky-Levich plots of PtP_2@PNC at the range potential from 0.3 to 0.7 V vs. RHE.

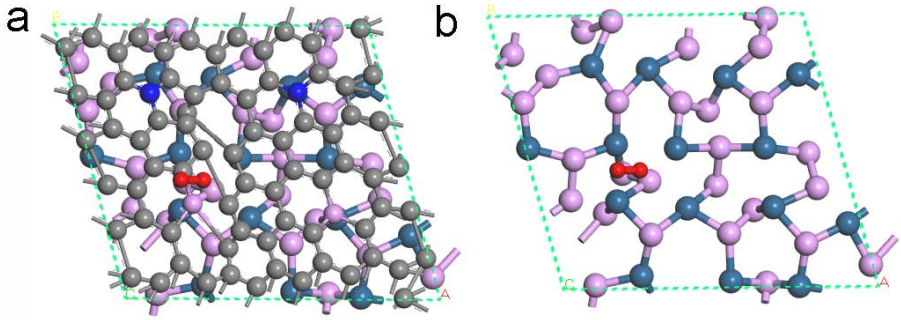

Figure S27. Models of oxygen adsorbed on (a) PtP_2@PNC and (b) PtP_2, related to Figure 5.

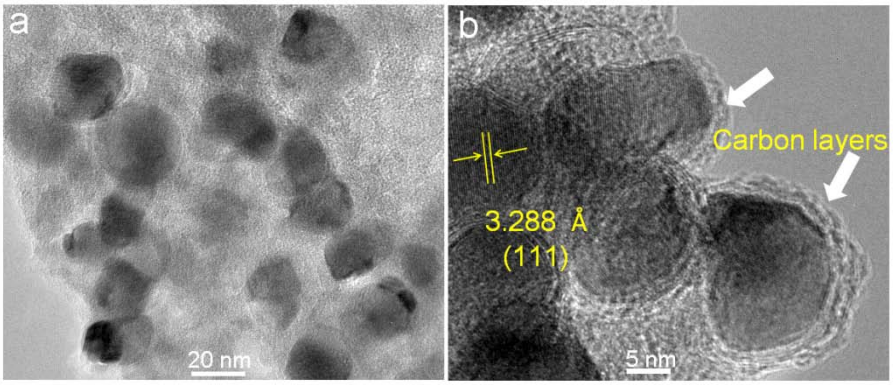

Figure S28. (a) TEM and (b) HRTEM images of post-HOR PtP_2@PNC, related to Figure 5.

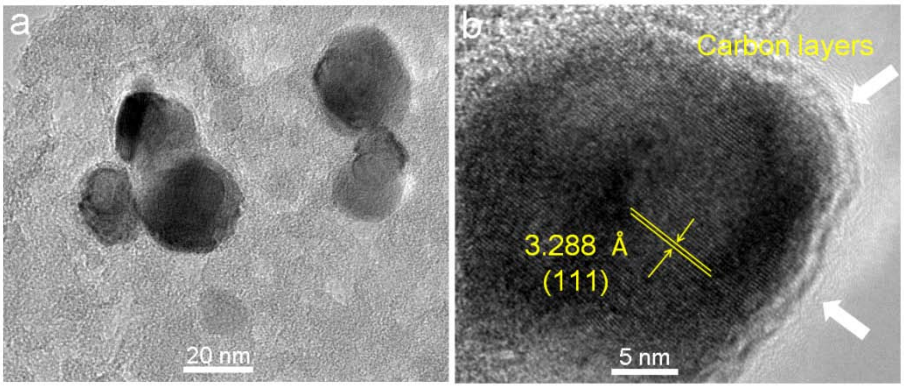

Figure S29. (a) TEM and (b) HRTEM images of post-ORR PtP_2@PNC, related to Figure 5.

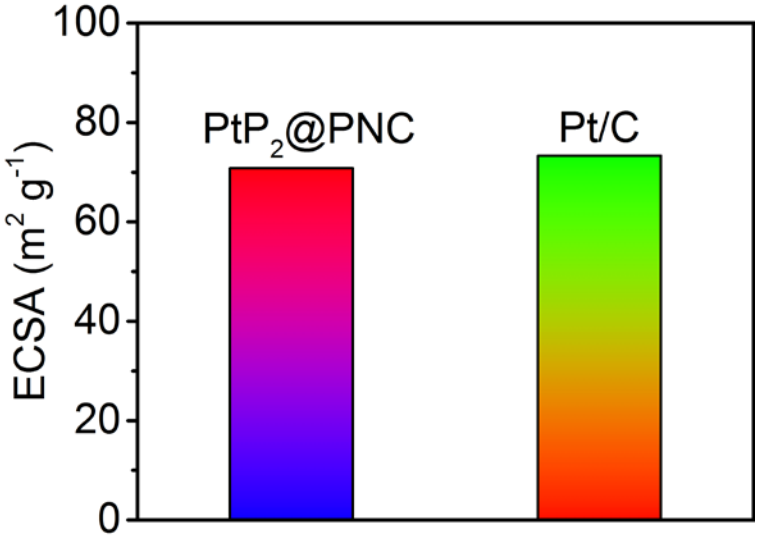

Figure S30. Histogram of ECSAs of PtP_2@PNC and Pt/C in 0.1 M $HClO_4$ solutions, related to Figure 5.

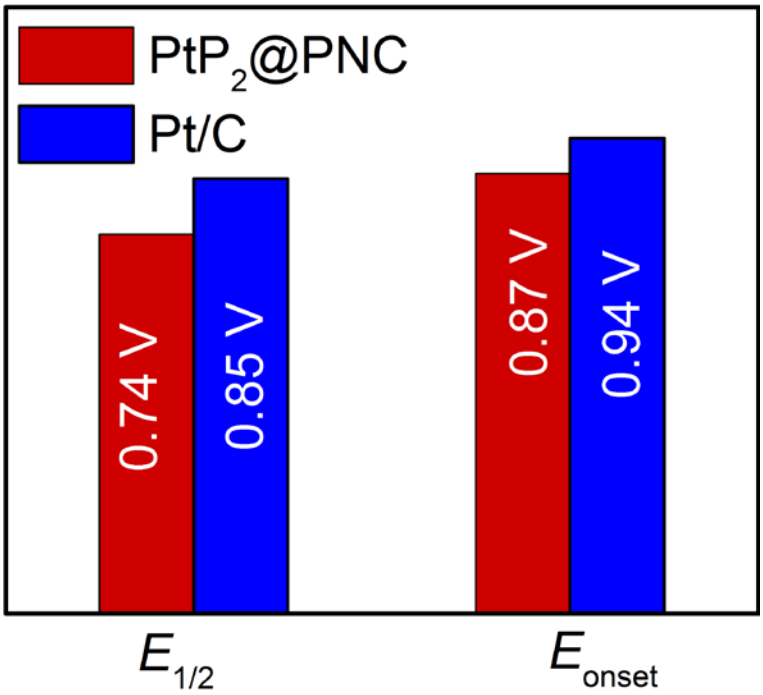

Figure S31. E_{onset} and $E_{1/2}$ comparison, related to Figure 5.

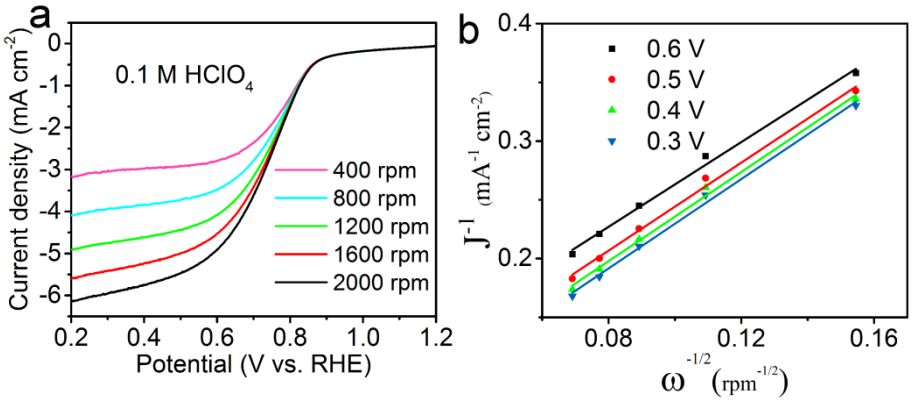

Figure S32. ORR performances of PtP_2@PNC a inacidic condition, related to Figure 5.
(a) LSV curves of PtP_2@PNC at different rotation speeds in 0.1 M $HClO_4$. (b) The Koutecky-Levich plots of PtP_2@PNC at the range potential from 0.3 to 0.6 V vs. RHE.

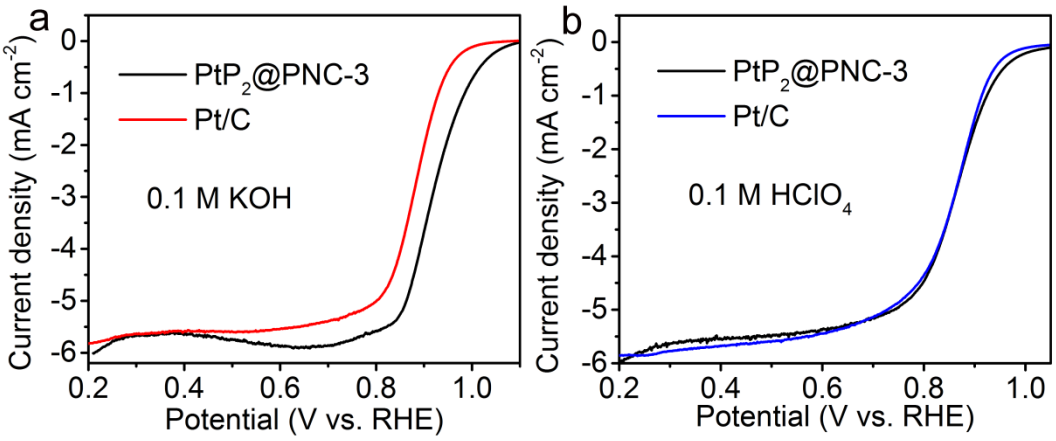

Figure S33. ORR performances of PtP_2@PNC in acidic and alkaline conditions, related to Figure 5.

LSV curves of PtP_2@PNC-3 (~24 wt% Pt) and commercial 20 wt% Pt/C at 5 mV s^{-1} at a rotating speed of 1600 rpm obtained in O_2-saturated (a) 0.1 M KOH and (b) 0.1 M $HClO_4$ solutions.

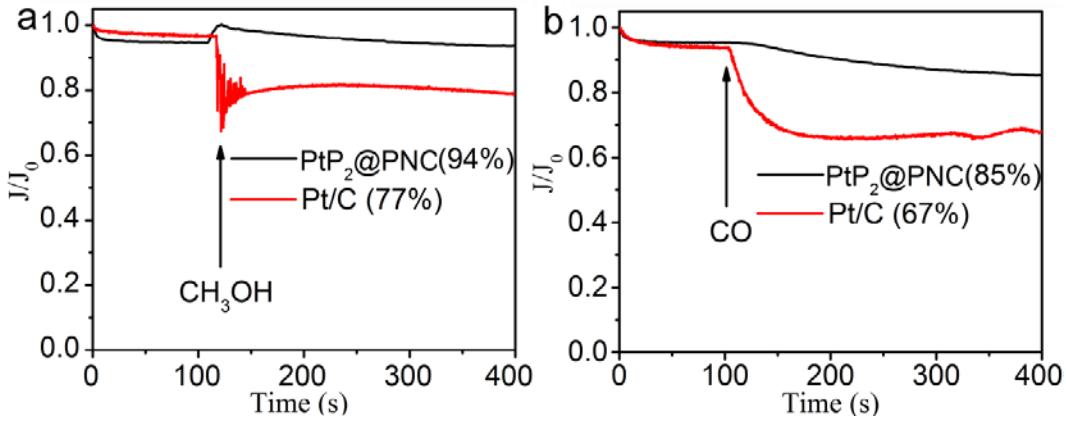

Figure S34. The i-t chronoamperometric curves for PtP_2@PNC and commercial 20 wt% Pt/C, related to Figure 5.

The i-t chronoamperometric responses for PtP_2@PNC and commercial 20 wt% Pt/C in (h) 3.0 M methanol O_2-saturated and (i) CO and O_2-saturated (V_{CO}/V_{O2}=10%) solution during a constant potential at 0.5 V at a rotation rate of 1,600 rpm in 0.1 M KOH.

Table S1 Comparison of HER performance in acid media for PtP_2@PNC with other HER electrocatalysts, related to Figure 4

Catalysts	Electrolytes	η@j (mV@mA cm^{-2})	Tafel slope (mV dec^{-1})	Loading (mg cm^{-2})	Ref.
PtP_2@PNC	0.5 M H_2SO_4	8@10	30	17.85 μgcm^{-2}_{Pt}	This work
Pt-MoS_2	0.1 M H_2SO_4	~150@10	96	18 μg cm^{-2}_{Pt}	Energy Environ. Sci. 8, 1594 (2017)
ALD50Pt/NGNs	0.5 M H_2SO_4	50@16	29	~1.6 μg cm^{-2}_{Pt}	Nat.Commun. 7, 13638 (2016)
400-SWMT/Pt	0.5 M H_2SO_4	27@10	38	~0.8 μg cm^{-2}_{Pt}	ACS Catal. 7, 3121 (2017)
Pt-GDY2	0.5 M H_2SO_4	~50@30	38	4.65 μg cm^{-2}_{Pt}	Angew. Chem. Int. Ed. 57, 9382 (2017)
Pt@PCM	0.5 M H_2SO_4	105@10	65.3	-	Sci. Adv. 4, eaao6657 (2018)
Pt-MoO_{3-x}	0.5 M H_2SO_4	23.3@10	28.8	~2 μg cm^{-2}_{Pt}	ChemCatChem 10, 946 (2016)
Pd/Cu-Pt NRs	0.5 M H_2SO_4	22.8@10	25	41 μg cm^{-2}	Angew. Chem., Int. Ed. 56, 16047 (2017)
CDs/Pt-PANI-4	0.5 M H_2SO_4	30@10	41.7	8.1μg cm^{-2}_{Pt}	Appl. Catal. B: Environ. 257, 117905 (2019)
Pd-MoS_2	0.5 M H_2SO_4	78@10	62	2.22 μg cm^{-2}_{Pd}	Nat. Commun. 9, 2120 (2018)
NiAu/Au	0.5 M H_2SO_4	~50@10	36	0.204	J. Am. Chem. Soc. 137, 5859 (2015)
Ru/C_3N_4/C	0.5 M H_2SO_4	~75@10	-	~0.2	J. Am. Chem. Soc. 138, 16174 (2016)
Ru/GO	0.5 M H_2SO_4	53@10	30	~0.1	ACS Appl. Mater. Interfaces 9, 3785 (2017)
Ru@C_2N	0.5 M H_2SO_4	22@10	30	0.285	Nat. Nanotechnol. 12, 441 (2017)
Rh_2P NPs	0.5 M H_2SO_4	14@10	31.7	4.59μg cm^{-2}_{Rh}	Adv. Energy Mater. 8, 1703489 (2018)
Rh/Si	0.5 M H_2SO_4	110@50	-	56μg cm^{-2}_{Rh}	Nat. Commun. 7,12272 (2016)
IrNi NCs	0.5 M H_2SO_4	32@20	-	12.5 μg cm^{-2}_{Ir}	Adv. Funct. Mater. 27, 1700886 (2017)
IrCo-PHNC	0.1 $HClO_4$	21@10	-	10.0 μg cm^{-2}_{Ir}	Adv. Mater. 29, 1703798 (2017)
RuP_2@NPC	0.5 M H_2SO_4	38@10	38	233 μg cm^{-2}_{Ru}	Angew. Chem., Int. Ed. 56, 11559 (2017)
PdP_2@CB	0.5 M H_2SO_4	27.5@10	29.5	18.5 μg cm^{-2}_{Pd}	Angew. Chem., Int. Ed. 57, 14862 (2018)
CoP/CC	0.5 M H_2SO_4	67@10	51	0.92	J. Am. Chem. Soc. 136, 7587 (2014)
MoP_2 NS/CC	0.5 M H_2SO_4	58@10	63.6	7.8	J. Mater. Chem. A 4, 7169 (2016)

MoP NA/CC	0.5 M H_2SO_4	124@10	58	2.5	Appl. Catal. B: Environ. 196, 193 (2016)
MoP_2 NPs/Mo	0.5 M H_2SO_4	143@10	57	~0.18	Nanoscale 8, 8500 (2016)
MoPNPs@NC	0.5 M H_2SO_4	115@10	65	2.0	Nanoscale 8, 17256 (2016)
FePNPs@NPC	0.5 M H_2SO_4	130@10	67	1.4	Nanoscale 9, 3555 (2017)
Mn-CoP/Ti	0.5 M H_2SO_4	49@10	55	5.61	ACS Catal. 7, 98 (2017)
$NiCo_2P_x$/CF	0.5 M H_2SO_4	104@10	59.6	5.9	Adv. Mater. 29, 1605502 (2017)
np-$(Co_{052}Fe_{0.48})_2P$	0.5 M H_2SO_4	64@10	45	-	Energy Environ. Sci. 9, 2257 (2016)
Ni_2P/Ti	0.5 M H_2SO_4	130@20	46	~1.0	J. Am. Chem. Soc. 135, 9267 (2013)
Ni_2P	0.5 M H_2SO_4	140@20	66	0.38	Phys. Chem. Chem. Phys. 16, 5917 (2014)
NiP_2 NS/CC	0.5 M H_2SO_4	75@10	51	4.3	Nanoscale 6, 13440 (2014)
CoP/CNT	0.5 M H_2SO_4	122@10	54	0.285	Angew. Chem., Int. Ed. 53, 6710 (2014)
CoP/Ti	0.5 M H_2SO_4	85@20	50	2.0	Angew. Chem., Int. Ed. 126, 5531 (2014)
FeP	0.5 M H_2SO_4	50@10	37	1.0	ACS Nano 8, 11101 (2014)
MoP	0.5 M H_2SO_4	180@30	54	0.86	Energy Environ. Sci. 7, 2624 (2014)
Co-NCNT/CC	0.5 M H_2SO_4	78@10	74	3.4	ChemSusChem 8, 1850 (2015)
CoNC/GD	0.5 M H_2SO_4	340@10	138	0.286	ACS Appl. Mater. Interfaces 8, 31083 (2016)
WN NA/CC	0.5 M H_2SO_4	198@10	62	2.5	Electrochimi. Acta 154, 345 (2015)
WON@NC	0.5 M H_2SO_4	106@10	65	7.8	ChemSusChem 8, 2487 (2015)
Mo_2C QD/NGCL	0.5 M H_2SO_4	136@10	68.4	2.0	Chem. Commun. 52, 12753 (2016)
P-W_2C@NC	0.5 M H_2SO_4	89@10	53	3.5	J. Mater. Chem. A 5, 765 (2017)
1D-RuO_2-CN_x	0.5 M H_2SO_4	93@10	40	-	ACS Appl. Mater. Interfaces 8, 28678 (2016)
Co-Ni-B	0.1 M $HClO_4$	209@10	-	2.1	Appl. Catal. B: Environ. 192, 126 (2016)
$Zn_{0.3}Co_{2.7}S_4$	0.5 M H_2SO_4	80@10	47.5	0.285	J. Am. Chem. Soc. 138, 1359 (2016)
CNF@CoS_2	0.5 M H_2SO_4	110@10	66.8	~8.88	Inorg. Chem. Front. 3, 1280 (2016)

Ni-C-N NSs	0.5 M H_2SO_4	60.9@10	32	0.2	J. Am. Chem. Soc.138, 14546 (2016)
Co-C-N	0.5 M H_2SO_4	138@10	55	-	J. Am. Chem. Soc.137, 15070 (2015)
Co-NRCNTs	0.5 M H_2SO_4	260@10	80	0.28	Angew. Chem., Int. Ed. 126, 4461 (2014)
Co-Mo-S_x	0.1 M $HClO_4$	~250@5	-	-	Nat. Mater. 15, 197 (2016)
NF/NiCoMoO-H_2	1.0 M KOH	15@10	33.1	2.7	Appl. Catal. B: Environ. 258, 117953 (2019)

Table S2 P concentration detected by ICP-AES after HER testing in H_2SO_4 solution, related to Figure 4.

Elemental	P
After HER electrolysis	8.9 ppb

Table S3 Comparison of HOR performance for PtP_2@PNC with other HOR electrocatalysts, related to Figure 5.

Catalyst	Loading (μg_{metal} cm^{-2})	Electrolyte	Exchange current density i_0(mA cm^{-2})	Ref.
PtP_2@PNC	8.93	0.1 M $HClO_4$	16.6 mA cm^{-2}_{Pt}	This work
Pd-CNx	43	0.1 M H_2SO_4	0.84	ACS Catal. 6, 1929 (2016)
Pd/C	5	0.1 M $HClO_4$	2.56mA cm^{-2}_{Pd}	J. Electrochem. Soc. 163, F499 (2016)
Pd/C-600C	30	0.1 M $HClO_4$	4.49mA cm^{-2}_{Pd}	J. Electrochem. Soc. 163, F499 (2016)
Pt/C	-	0.1 M H_2SO_4	24 mA cm^{-2}_{Pt}	J. Phys. Chem. B 108, 13984 (2004)
Pt	-	0.1 M $HClO_4$	~42	J. Phys. Chem. B 2003, 107, 6401 (2003)
PdIr/C	35	1 M KOH	0.98	J. Electrochem. Soc. 161, 458 (2014)
Ir3PdRu6/C	3.5	0.1 M KOH	0.6	J. Am. Chem. Soc. 139, 6807 (2017)
Ru3Ir2/C	7.8	0.1 M NaOH	0.85	J. Mater. Chem. A 4, 15980 (2016)
Ir/C-800	10	0.1 M KOH	0.5	ACS Catal. 5, 4449 (2015)

Table S4 Comparison of the ORR activity of PtP_2@PNC with other electrocatalysts previously reported, related to Figure 5.

Catalyst	Mass/specific activity @ 0.9V	$E_{1/2}$ (V)	Electrolyte	Loading (mg cm^{-2})	Ref.
PtP_2@PNC	148.6 $mA \cdot mg^{-1}_{Pt}$	0.82	0.1 M KOH	0.15	This work
Fe_3Pt	-	0.91	0.1 M KOH	0.12	Angew. Chem. Int. Ed. 56, 9901 (2017)
Fe_3Pt/Ni_3FeN	351.6 $mA \cdot mg^{-1}_{Pt}$	0.93	0.1 M KOH	0.12	Angew. Chem. Int. Ed. 56, 9901 (2017)
Pd_3Pd/C	168.9 $mA \cdot mg^{-1}_{Pd}$	0.92	0.1 M KOH	0.125	Nano Lett. 16, 2560 (2016)
PdMo bimetallence	16.37 A mg^{-1}_{Pt}	0.95	0.1 M KOH	7.5μg_{metal}	Nature 574, 81 (2019)
Pd-P	1.34 A mg^{-1}_{Pt} @0.85 V	0.88	0.1 M KOH	-	J. Am. Chem. Soc. 136, 5217 (2014)
CNT-grphene	-	0.87	0.1 M KOH	0.485	Nat. Nanotechnol. 7, 394
Co_3O_4/N-rmGO	-	0.83	0.1 M KOH	0.17	Nat. Mater. 10, 780 (2011)
Co_2P	-	-0.196 vs. Ag/AgCl)	0.1 M KOH	-	ACS Nano 9, 8108 (2015)
Fe-P	-	~0.8	0.1 M KOH	39.5 μg cm^{-2}	J. Am. Chem. Soc. 137, 3165 (2015)
Cu_3P@NPPC	-	0.78	0.1 M KOH	0.2	Adv. Mater. 30, 1703711 (2018)
IrP_2/NPC	-	0.89	0.1 M KOH	1.6μg_{Ir}	ACS Appl. Mater. Interfaces 11, 16461 (2019)
Rh_xP/NPC	-	0.89	0.1 M KOH	0.94	Adv. Energy Mater. 8, 1801478 (2018)
Pt on Pd	307 μAcm^{-2}_{Pt}	-	0.1 M $HClO_4$	-	J. Am. Chem. Soc. 131, 7542 (2009)
PtNi NWs	2.97 A mg^{-1}_{Pt}	-	0.1 M $HClO_4$	1.25 μg_{Pt}	Sci. Adv. 3, e1601705 (2017)
FePtPd/FePt NWs	1.68 A mg^{-1}_{Pt}(@0.5 V vs.Ag/AgCl)	-	0.1 M $HClO_4$	-	J. Am. Chem. Soc. 135, 13879 (2013)

References

Deng, J., Li, H. B., Xiao, J. P., Tu, Y. C., D. Deng, H.,Yang, H. X., Tian, H. F., Li, J. Q., Ren, P. J. And Bao,X. H. (2015). Triggering the electrocatalytic hydrogen evolution activity of the inert two-dimensional MoS_2 surface via single-atom metal doping. *Energy Environ. Sci. 8*, 1594–1601.

Cheng, N., Stambula, S., Wang, D., Banis, M. N., Liu, J., Riese, A., Xiao, B., Li, R., Sham, T. K., Liu, L., Botton, G. A. and Sun, X. (2016). Platinum single-atom and cluster catalysis of the hydrogen evolution reaction. *Nat.Commun. 7*, 13638.

Tavakkoli, M., Holmberg, N., Kronberg, R., Jiang, H., Sainio, J., Kauppinen, E. I., Kallio,T., Laasonen, K. (2017). Electrochemical activation of single-walled carbon nanotubes with pseudo-atomic-scale platinum for the hydrogen evolution reaction. *ACS Catal. 7*, 3121–3130.

Yin, X., Wang, H., Tang, S., Lu, X., Shu, M., Si, R. and Lu, T. (2018). Engineering the coordination environment of single‐atom platinum anchored on graphdiyne for optimizing electrocatalytic hydrogen evolution. *Angew. Chem., Int. Ed. 57,* 9382–9386.

Zhang, H., An, P., Zhou, W., Guan, B. Y., Zhang, P., Dong, J. and Lou, X. W. (2018). Dynamic traction of lattice-confined platinum atoms into mesoporous carbon matrix for hydrogen evolution reaction. *Sci. Adv. 4*, eaao6657.

Liu, W., Xu, Q., Yan, P. F., Chen, J., Du, Y., Chu, S. Q. and Wang, J. O. (2018). Fabrication of a single-atom platinum catalyst for the hydrogen evolution reaction: A new protocol by utilization of H_xMoO_{3-x} with plasmon resonance. *ChemCatChem 10*, 946–950.

Chao, T. T., Luo, X., Chen, W. X., Jiang, B., Ge, J. J., Lin, Y., Wu, G., Wang, X. Q., Hu, Y. M., Zhuang, Z. B., Wu, Y., Hong, X. and Li, Y. D. (2017). Atomically dispersed copper–platinum dual sites alloyed with palladium nanorings catalyze the hydrogen evolution reaction. *Angew. Chem., Int. Ed. 56*, 16047–16051.

Dang, Q., Sun, Y., Wang, X., Zhu, W., Chen, Y., Liao, F., Huang, H. and Shao, M. (2019). Carbon dots-Pt modified polyaniline nanosheet grown on carbon cloth as stable and high-efficient electrocatalyst for hydrogen evolution in pH-universal electrolyte. *Appl. Catal. B: Environ. 257*, 117905.

Luo, Z., Ouyang, Y., Zhang, H., Xiao, M., Ge, J., Jiang, Z., Wang, J., Tang, D., Cao, X., Liu, C. and Xing, W. (2018). Chemically activating MoS_2 via spontaneous atomic palladium interfacial doping towards efficient hydrogen evolution. *Nat. Commun. 9*, 2120.

Lv, H., Xi, Z., Chen, Z., Guo, S., Yu, Y., Zhu, W., Li, Q., Zhang, X., Pan, M., Lu, G., Mu, S. and Sun, S. (2015). A new core/shell NiAu/Au nanoparticle catalyst with Pt-like activity for hydrogen evolution reaction.*J. Am. Chem. Soc. 137*, 5859–5862.

Zheng, Y., Jiao, Y., Zhu, Y., Li, L., Han, Y., Chen, Y., Jaroniec, M. and Qiao, S. (2016). High electrocatalytic hydrogen evolution activity of an anomalous ruthenium catalyst. *J. Am. Chem. Soc. 138*, 16174–16181.

Ye, R.,Liu, Y., Peng, Z., Wang, T., Jalilov, A. S., Yakobson, B. I., Wei, S. and Tour, J. M. (2017). High performance electrocatalytic reaction of hydrogen and oxygen on ruthenium nanoclusters. *ACS Appl. Mater. Interfaces 9*, 3785−3791.

Mahmood, J., Li, F., Jung, S., Okyay, M. S., Ahmad, I., J.Kim, S., Park, N., Jeong, H. Y. and Baek, J. B. (2017). An efficient and pH-universal ruthenium-based catalyst for the hydrogen evolution reaction. *Nat. Nanotechnol. 12*, 441–446.

Yang, F., Zhao, Y., Du, Y., Chen, Y., Cheng, G., Chen, S. and Luo, W. (2018). A monodisperse Rh_2P-based electrocatalyst for highly efficient and pH-universal hydrogen evolution reaction. *Adv. Energy Mater. 8***,** 1703489.

Zhu, L., Lin, H., Li, Y., Liao, F., Lifshitz, Y., Sheng, M., Lee, S. T and Shao, M. (2016). A rhodium/silicon co-electrocatalyst design concept to surpass platinum hydrogen evolution activity at high overpotentials. *Nat. Commun. 7*,12272.

Pi, Y., Shao, Q., Wang, P., Guo, J. and Huang, X. (2017). General formation of monodisperse IrM (M= Ni, Co, Fe) bimetallic nanoclusters as bifunctional electrocatalysts for acidic overall water splitting. *Adv. Funct. Mater. 27*, 1700886.

Feng, J., Lv, F., Zhang, W., Li, P., Wang, K., Yang, C., Wang, B., Yang, Y., Zhou, J., Lin, F., Wang, G. and Guo, S. (2017). Iridium-based multimetallic porous hollow nanocrystals for efficient overall‐water‐splitting catalysis. *Adv. Mater. 29*, 1703798.

Pu, Z., Amiinu, I. S., Kou, Z., Li, W. and Mu, S. (2017). RuP_2-based catalysts with platinum-like activity and higher durability for the hydrogen evolution reaction at all pH-values. *Angew. Chem., Int. Ed.* 56, 11559.

Luo, F., Zhang, Q., Yu, X., Xiao, S., Ling, Y., Hu, H., Guo, L, Yang, Z., Huang, L., Cai, W. and Cheng, H. (2018). Palladium phosphide as a stable and efficient electrocatalyst for overall water splitting.*Angew. Chem., Int. Ed. 57*, 14862-14867.

Tian, J., Liu, Q., Asiri, A. M. and Sun, X. (2014). Self-supported nanoporous cobalt phosphide nanowire arrays: an efficient 3D hydrogen-evolving cathode over the wide range of pH 0–14. *J. Am. Chem. Soc. 136*, 7587–7590.

Zhu, W., Tang, C., Liu, D., Wang, J., Asiri, A. M. and Sun, X. (2016). A self-standing nanoporous MoP_2 nanosheet array: an advanced pH-universal catalytic electrode for the hydrogen evolution reaction. *J. Mater. Chem. A 4*, 7169–7173.

Pu, Z., Wei, S., Chen, Z. and Mu, S. (2016). Flexible molybdenum phosphide nanosheet array electrodes for hydrogen evolution reaction in a wide pH range. *Appl. Catal. B: Environ. 196,* 193–198.

Pu, Z., Amiinu, I. S., Wang, M., Yang, Y. and Mu, S. (2016). Semimetallic MoP_2: an active and stable hydrogen evolution electrocatalyst over the whole pH range. *Nanoscale 8*, 8500–8504.

Pu, Z., Amiinu, I. S., Liu, X., Wang, M. and Mu, S. (2016). Ultrastable nitrogen-doped carbon encapsulating molybdenum phosphide nanoparticles as highly efficient electrocatalyst for hydrogen generation. *Nanoscale 8*, 17256–17261.

Pu, Z., Xue, Y., Amiinu, I. S., Zhang, C., Wang, M., Kou, Z. and Mu, S. (2017). Phytic acid-derivative transition metal phosphides encapsulated in N,P-codoped carbon: an efficient and durable hydrogen evolution electrocatalyst in a wide pH range. *Nanoscale 9*, 3555–3560.

Liu, T., Ma, X., Liu, D., Hao, S., Du, G., Ma, Y., Asiri. A. M., Sun, X. and Chen, L. (2017). Mn doping of CoP nanosheets array: an efficient electrocatalyst for hydrogen evolution reaction with enhanced activity at all pH values. *ACS Catal. 7*, 98–102.

Zhang, R., Wang, X., Yu, S., Wen, T., Zhu, X., Yang, F., Sun, X., Wang, X. and Hu, W. (2017). Ternary $NiCo_2P_x$nanowires as pH-universal electrocatalysts for highly efficient hydrogen evolution reaction. *Adv. Mater. 29*, 1605502.

Tan, Y., Wang, H., Liu, P., Shen, Y., Cheng, C., Hirata, A., Fujita, T., Tang, Z.and Chen, M. (2016). Versatile nanoporous bimetallic phosphides towards electrochemical water splitting. *Energy Environ. Sci. 9*, 2257–2261.

Popczun, E. J., McKone, J. R., Read, C. G., Biacchi, A. J., Wiltrout, A. M., Lewis, N. S. and Schaak, R. E. (2013). Nanostructured nickel phosphide as an electrocatalyst for the hydrogen evolution reaction. *J. Am. Chem. Soc. 135*, 9267–9270.

Feng, L., Vrubel, H., Bensimon, M. and Hu, X. (2014). Easily-prepared dinickel phosphide (Ni_2P) nanoparticles as an efficient and robust electrocatalyst for hydrogen evolution. *Phys. Chem. Chem. Phys. 16*, 5917–5921.

Jiang, P., Liu, Q. and Sun, X. (2014). NiP_2 nanosheet arrays supported on carbon cloth: an efficient 3D hydrogen evolution cathode in both acidic and alkaline solutions. *Nanoscale 6*, 13440–13445.

Liu, Q., Tian, J., Cui, W., Jiang, P., Cheng, N, Asiri, A. M. and Sun, X. (2014). Carbon nanotubes decorated with CoP nanocrystals: a highly active non-noble-metal nanohybrid electrocatalyst for hydrogen evolution. *Angew. Chem., Int. Ed. 53*, 6710–6714.

Popczun, E. J., G.Read, C., Roske, C. W., Lewis, N. S.and Schaak, R. E. (2014). Highly active electrocatalysis of the hydrogen evolution reaction by cobalt phosphide nanoparticles. *Angew. Chem., Int. Ed. 126*, 5531–5534.

Juan, F., Callejas, J., McEnaney, M., Read, C. G., Crompton, J. C., Biacchi, A. J., Popczun, E. J., Gordon, T. R., Lewis, N. S. and Schaak, R. E. (2014). Electrocatalytic and photocatalytic hydrogen production from acidic and neutral-pH aqueous solutions using iron phosphide nanoparticles. *ACS Nano 8*, 11101–11107.

Xiao, P., Sk, M. A., Thia, L., Ge, X., Lim, R. J., Wang, J. Y., Lim, K. H. and Wang, X. (2014). Molybdenum phosphide as an efficient electrocatalyst for the hydrogen evolution reaction. *Energy Environ. Sci. 7*, 2624–2629.

Xing, Z., Liu, Q., Xing, W., Asiri, A. M. and Sun, X. (2015). Interconnected Co-entrapped, N-doped carbon nanotube film as active hydrogen evolution cathode over the whole pH range. *ChemSusChem 8*, 1850–1855.

Xue, Y., Li, J., Xue, Z., Li, Y., Liu, H., Li, D., Yang, W. and Li, Y. (2016). Extraordinarily durable graphdiyne-supported electrocatalyst with high activity for hydrogen production at all values of pH. *ACS Appl. Mater. Interfaces 8*, 31083−31091.

Shi, J., Pu, Z., Liu, Q., Asiri, A. M., Hu, J. and Sun, X. (2015). Tungsten nitride nanorods array grown on carbon cloth as an efficient hydrogen evolution cathode at all pH values. *Electrochimi. Acta 154*, 345–351.

Li, Q., Cui, W., Tian, J., Xing, Z., Liu, Q., Xing, W., Asiri, A. M. and Sun, X. (2015). N-Doped carbon-coated tungsten oxynitride nanowire arrays for highly efficient electrochemical hydrogen evolution. *ChemSusChem 8*, 2487–2491.

Pu, Z., Wang, M., Kou, Z., Amiinu, I. S. and Mu, S. (2016). Mo_2C quantum dot embedded chitosan-derived nitrogen-doped carbon for efficient hydrogen evolution in a broad pH range. *Chem. Commun. 52*, 12753–12756.

Yan, G., Wu, C., Tan, H., Feng, X., Yan, L., Zang, H. and Li, Y. (2017). N-Carbon coated P-W_2C composite as efficient electrocatalyst for hydrogen evolution reactions over the whole pH range. *J. Mater. Chem. A 5*, 765–772.

Bhowmik, T., Kundu, M. and Barman, S. (2016). Growth of one-dimensional RuO_2 nanowires on g-carbon nitride: an active and stable bifunctional electrocatalyst for hydrogen and oxygen evolution reactions at all pH values. *ACS Appl. Mater. Interfaces 8*, 28678−28688.

Gupta, S., Patela, N., Fernandes, R., Kadrekar, R., Dashora, A., Yadav, A. K., Bhattacharyya,

D., Jha, S. N., Miotello, A. and Kothari, D. C. (2016). Co–Ni–B nanocatalyst for efficient hydrogen evolution reaction in wide pH range. *Appl. Catal. B: Environ*. *192*, 126–133.

Huang, Z., Song, J., Li, K., Tahir, M., Wang, Y., Pan, L., Wang, L., Zhang, X., Zou, J. (2016). Hollow cobalt-based bimetallic sulfide polyhedra for efficient all-pH-value electrochemical and photocatalytic hydrogen evolution. *J. Am. Chem. Soc. 138*, 1359–1365.

Gu, H., Huang, Y., Zuo, L., Fan, W. and Liu, T. (2016). Electrospun carbon nanofiber@ CoS_2 core/sheath hybrid as an efficient all-pH hydrogen evolution electrocatalyst. *Inorg. Chem. Front. 3*, 1280–1288.

Yin, J., Fan, Q., Li, Y., Cheng, F., Zhou, P., Xi, P. and Sun, S. (2016). Ni–C–N nanosheets as catalyst for hydrogen evolution reaction. *J. Am. Chem. Soc.138*, 14546–14549.

Wang, S., Hao, X., Jiang, Z., Sun, X., Xu, D., Wang, J., Zhong, H., Meng, F. and Zhang, X. (2015). C and N hybrid coordination derived Co–C–N complex as a highly efficient electrocatalyst for hydrogen evolution reaction. *J. Am. Chem. Soc.137*, 15070–15073.

Zou, X., Huang, X., Goswami, A., Silva, R., Sathe, B. R., Mikmekova, E. and Asefa, T. (2014). Cobalt-embedded nitrogen-rich carbon nanotubes efficiently catalyze hydrogen evolution reaction at all pH values. *Angew. Chem., Int. Ed. 126*, 4461–4465.

Jirkovský, J. S., Malliakas, C. D., Lopes, P. P., Danilovic, N., Kota, S. S., Chang, K. C., Genorio, B., Strmcnik, D., Stamenkovic, V. R., Kanatzidis, M. G., Markovic, N. M. (2016). Design of active and stable Co–Mo–S_x chalcogels as pH-universal catalysts for the hydrogen evolution reaction. *Nat. Mater. 15*, 197–203.

Wen, S., Yang, T., Zhao, N., Ma, L. and Liu, E. (2019). Ni-Co-Mo-O nanosheets decorated with NiCo nanoparticles as advanced electrocatalysts for highly efficient hydrogen evolution. *Appl. Catal. B: Environ. 258*, 117953.

Bhowmik, T., Kundu, M. K. and Barman, S. (2016). Palladium nanoparticle–graphitic carbon nitride porous synergistic catalyst for hydrogen evolution/oxidation reactions over a broad range of pH and correlation of its catalytic activity with measured hydrogen binding energy. *ACS Catal. 6*, 1929−1941.

Zheng, J., Zhou, S., Gu, S., Xu, B. and Yan, Y. (2016). Size-dependent hydrogen oxidation and evolution activities on supported palladium nanoparticles in acid and base. *J. Electrochem. Soc. 163*, F499-F506.

Chen, S. L., Kucernak, A. (2004). Electrocatalysis under conditions of high mass transport: Investigation of hydrogen oxidation on single submicron Pt particles supported on carbon. *J. Phys. Chem. B 108*, 13984-13994.

Zoski, C. G. (2003). Scanning electrochemical microscopy: investigation of hydrogen oxidation at polycrystalline noble metal electrodes. *J. Phys. Chem. B 107*, 6401-6405.

Jervisa, R., Mansora, N., Gibbsa, C., Murrayd, C. A., Tangd, C. C., Shearing P. R. and Brett, D. J. L. (2014). Hydrogen oxidation on PdIr/C catalysts in alkaline media. *J. Electrochem. Soc. 161*, 458-463.

Wang, H. and Abruña, H. D. (2017). IrPdRu/C as H_2 oxidation catalysts for alkaline fuel cells. *J. Am. Chem. Soc. 139*, 6807–6810.

Ohyama, J., Kumadaa, D. and Satsuma, A. (2016). Improved hydrogen oxidation reaction under alkaline conditions by ruthenium–iridium alloyed nanoparticles. *J. Mater. Chem. A 4*, 15980.

Zheng, J., Zhuang, Z., Xu, B. and Yan, Y. (2015). Correlating hydrogen oxidation/evolution

reaction activity with the minority weak hydrogen-binding sites on Ir/C catalysts. *ACS Catal. 5*, 4449−4455.

Cui, Z., Fu, G., Li, Y. and Goodenough, J. B. (2017). Ni_3FeN-supported Fe_3Pt intermetallic nanoalloy as a high-performance bifunctional catalyst for metal-air batteries. *Angew. Chem. Int. Ed. 56*, 9901–9905.

Cui, Z., Chen, H., Zhao, M. and DiSalvo, F. J. (2016). High-performance Pd_3Pb intermetallic catalyst for electrochemical oxygen reduction. *Nano Lett. 16*, 2560−2566.

Luo, M., Zhao, Z., Zhang, Y., Sun, Y., Xing, Y., Lv, F., Yang, Y., Zhang, X., Hwang, S., Qin, Y., Ma, J., Lin, F., Su, D., Lu, G. and Guo, S. (2019). PdMo bimetallene for oxygen reduction catalysis. *Nature 574*, 81-85.

Poon, K. C., Tan, D. C. L., Vo, T. D.T., Khezri, B., Su, H., Webster, R. D. and Sato, H. (2014). Newly developed stepwise electroless deposition enables a remarkably facile synthesis of highly active and stable amorphous Pd nanoparticle electrocatalysts for oxygen reduction reaction. *J. Am. Chem. Soc. 136*, 5217-5220.

Li, Y., Zhou, W., Wang, H., Xie, L., Liang, Y., Wei, F., Idrobo, J. C., Pennycook, S. J. and Dai, H. (2012). An oxygen reduction electrocatalyst based on carbon nanotube–graphene complexes. *Nat. Nanotechnol. 7*, 394–400.

Liang, Y., Li, Y., Wang, H., Zhou, J., Wang, J., Regier and, T. and Dai, H. (2011). Co_3O_4 nanocrystals on graphene as a synergistic catalyst for oxygen reduction reaction. *Nat. Mater. 10*, 780-786.

Doan-Nguyen, V. V. T., Zhang, S., Trigg, E. B., Agarwal, R., Li, J., Su, D., Winey, K. I. and Murray, C. B. (2015). Synthesis and X-ray characterization of cobalt phosphide (Co_2P) nanorods for the oxygen reduction reaction. *ACS Nano 9*, 8108-8115.

Singh, K. P., Bae, E. J. and Yu, J. (2015). Fe–P: a new class of electroactive catalyst for oxygen reduction reaction. *J. Am. Chem. Soc. 137*, 3165-3168.

Wang, R., Dong, X., Du, J., Zhao, J. and Zang, S. (2018). MOF-derived bifunctional Cu_3P nanoparticles coated by a N,P-codoped carbon shell for hydrogen evolution and oxygen reduction.*Adv. Mater. 30*, 1703711.

Qin, Q., Jang, H., Chen, L., Li, P., Wei, T., Liu X. and Cho, J. (2019). Coupling a low loading of IrP_2, PtP_2, or Pd_3P with heteroatom-doped nanocarbon for overall water-splitting cells and zinc–air batteries. *ACS Appl. Mater. Interfaces 11*, 16461-16473.

Qin, Q., Jang, H., Chen, L., Nam, G., Liu, X. and Cho, J. (2018). Low loading of Rh_xP and RuP on N, P codoped carbon as two trifunctional electrocatalysts for the oxygen and hydrogen electrode reactions. *Adv. Energy Mater. 8*, 1801478.

Peng, Z. and Yang, H. (2009). Synthesis and oxygen reduction electrocatalytic property of Pt-on-Pd bimetallic heteronanostructures. *J. Am. Chem. Soc. 131*, 7542-7543.

Jiang, K., Zhao, D., Guo, S., Zhang, X., Zhu, X., Guo, J., Lu, G. and Huang, X. (2017). Efficient oxygen reduction catalysis by subnanometer Pt alloy nanowires. *Sci. Adv*. *3*, e1601705.

Guo, S., Zhang, S., Su, D. and Sun, S. (2013). Seed-mediated synthesis of core/shell FePtM/FePt (M= Pd, Au) nanowires and their electrocatalysis for oxygen reduction reaction. *J. Am. Chem. Soc. 135*, 13879–13884.